POLITECNICO DI TORINO
Repository ISTITUZIONALE

Euler-Lagrange modeling of circular discrete orifices gas-liquid pintle injectors using blob injection

Original
Euler-Lagrange modeling of circular discrete orifices gas-liquid pintle injectors using blob injection / Stumpo, L., Ferrero, A., Masseni, F., Pastrone, D.. - In: AEROSPACE SCIENCE AND TECHNOLOGY. - ISSN 1270-9638. - 180:(2027). [10.1016/j.ast.2026.113675]

Availability:
This version is available at: 11583/3016872 since: 2026-10-22T10:45:52Z

Publisher:
Elsevier Masson

Published
DOI:10.1016/j.ast.2026.113675

Terms of use:

This article is made available under terms and conditions as specified in the corresponding bibliographic description in the repository

Publisher copyright

(Article begins on next page)

18 November 2026

Aerospace Science and Technology 180 (2027) 113675

Contents lists available at ScienceDirect

Aerospace Science and Technology

journal homepage: www.elsevier.com/locate/aescte

Original article

Euler-Lagrange modeling of circular discrete orifices gas-liquid pintle injectors using blob injection

Leonardo Stumpo*, Andrea Ferrero, Filippo Masseni, Dario Pastrone

DIMEAS, Politecnico di Torino, Corso Duca degli Abruzzi 24, Turin, 10129, TO, Italy

ARTICLE INFO

Communicated by Dr Mehdi Ghoreyshi

Keywords:
Gas-liquid pintle
Rocket engines
Euler-Lagrange
Crossflow
Spray breakup

ABSTRACT

An Euler-Lagrange methodology under Unsteady Reynolds-Averaged Navier-Stokes closure is proposed for cold-flow atomization in gas-liquid pintle injectors with discrete circular orifices. No interface-resolving treatment of the primary breakup region is employed: blob injection initializes the dispersed phase, and the Madabhushi model governs the complete atomization cascade. Model constants are determined a priori from literature values and correlations as a function of the operating condition; in particular, the column-breakup constant is tied to operating-condition correlations rather than treated as a free parameter, which reduces the uncertainty associated with the breakup-model calibration with respect to a single, case-independent value.

The approach is validated against four test configurations encompassing two sets of experimental Sauter mean diameter measurements at different ambient pressures and two LES VOF-to-DPM reference solutions at $We_g = 3500$ and 8500. The radial Sauter Mean Diameter profiles are reproduced with good accuracy across all downstream stations; locally, the model tends to overpredict D_{32} in the near-field and near-axis region and to underpredict it in the far field. As far as the comparison with LES is concerned, good agreement is obtained at $We_g = 3500$ and 8500 for the diameter distributions, percentile diameters, and droplet velocity profiles, with local point-wise deviations along the transverse profiles. A preliminary effective column-phase drag correction is assessed through a ±30% sensitivity study based on the spatially resolved transverse diameter profiles. Among the investigated values, the nominal coefficient provides the most consistent profile agreement, yielding the lowest D_{32}-profile NRMSE at both Weber numbers without a systematic benefit from a further increase. The correction is therefore retained as a preliminary effective-area projected closure for the present conditions rather than as a final or universal drag correlation. The results confirm that the proposed framework provides a physically consistent and computationally efficient description of spray statistics in pintle injectors across a wide throttling range, enabling a faster design with respect to interface- or scale-resolving methods.

1. Introduction

The pintle injector, first developed at the Jet Propulsion Laboratory (JPL) of the California Institute of Technology in the mid-1950s [1], has played a key role in the evolution of variable-thrust rocket engines. Thanks to its simple design, combustion stability, and high throttling capability, it was adopted in several historical propulsion systems such as the Apollo Lunar Module Descent Engine (LMDE), the SpaceX Merlin series, and the TR-106 engine family [2]. Throttling in pintle injectors is typically achieved by axially moving the pintle tip relative to the surrounding sleeve or orifice plate [3], thereby modulating the effective flow area and adjusting the momentum ratio between the radial and axial streams. This mechanical actuation enables wide-range thrust variation while maintaining stable combustion conditions, making the pintle injector particularly suitable for reusable and throttleable engines.

In its conventional configuration, one propellant is injected axially through an annular passage surrounding the central pintle, while the other is discharged radially from the pintle tip [3]. The impingement between the axial and radial streams promotes efficient atomization and mixing within the combustion chamber. These characteristics make the pintle injector attractive not only for throttled engines but also for fixed-thrust systems that demand high combustion efficiency, mechanical simplicity, and robustness under a wide range of operating conditions. However, despite its practical advantages, the internal flow structure and atomization behavior of pintle injectors remain complex and highly sensitive to geometry [3–5], operating pressure [6], and momentum ratio [7,8]. Moreover, the spray distribution strongly influences wall heat fluxes, a critical aspect in pintle-based combustion chambers due to their inherently asymmetric spray pattern and localized thermal loads [9–12].

* Corresponding author.
E-mail address: leonardo.stumpo@polito.it (L. Stumpo).

https://doi.org/10.1016/j.ast.2026.113675
Received 5 June 2026; Received in revised form 10 August 2026; Accepted 20 August 2026
Available online 31 August 2026
1270-9638/© 2026 The Author(s). Published by Elsevier Masson SAS. This is an open access article under the CC BY license (http://creativecommons.org/licenses/by/4.0/).

Nomenclature

Latin symbols

a	parent parcel radius
A_p, A_{col}	projected areas (sphere, column)
B_0	Wave child-size constant
B_1	Wave breakup-time constant
C_0	column breakup-time constant
C_d, $C_{\text{D,eff}}$	drag coefficients
$C_{\text{D,col}}$	liquid-column drag coefficient
C_ω	rotational drag coefficient
c_p	specific heat
d	orifice diameter
d_p	particle diameter
D_0	blob (nozzle) diameter
D_{ref}, D_{cb}	reference, column-breakup diameter
D_{32}	Sauter mean diameter (SMD)
D_{10}	arithmetic mean diameter
d_{10}, d_{50}, d_{90}	percentile diameters
e, h	internal energy, enthalpy
F_{lig}	ligament factor
$\vec{F}$, $\vec{F}_e$	external forces
I, I_p	identity tensor, moment of inertia
k, k_{eff}	turbulent kinetic energy, conductivity
L	gas-film length
L_s	jump distance
$\dot{m}$	mass flow rate
m_p	particle mass
N_i	number of drops in size range i
p, p_a	pressure, ambient pressure
q	momentum-flux ratio
r	child-particle radius
S_m, S_h	mass, energy source terms
t	time
t_{cb}, t^*	column-breakup, reference time
t_{def}, t_b	deformation, total breakup time
T	temperature
$\vec{u}_p$, u_{rel}	particle velocity, relative velocity
U	mean axial droplet velocity
$\vec{v}$	gas velocity
W	gas-film height
x, z	axial, wall-normal coordinate
y^+	wall coordinate

Greek symbols

α	child normal-velocity angle
Δt, Δz	time step, bin size
ϵ	integration tolerance
Λ, Ω	KH wavelength, growth rate
μ, μ_l	gas, liquid dynamic viscosity
ν_l	liquid kinematic viscosity
ρ, ρ_p, ρ_l, ρ_g	densities
σ	surface tension
τ_r, τ	relaxation, breakup time
$\bar{\bar{\tau}}$	viscous stress tensor
$\vec{\Omega}$	relative angular velocity
$\vec{\omega}_p$	particle angular velocity

Dimensionless groups

Oh	Ohnesorge number
Re, Re_l, Re_j	Reynolds numbers
Re_ω	rotational Reynolds number
Ta	Taylor number
We, We_g, We_l	Weber numbers
We_{corr}, We_{aero}	corrected, aerodynamic Weber numbers

Acronyms

CFD	Computational Fluid Dynamics
DPM	Discrete Phase Model
DRW	Discrete Random Walk
EWT	Enhanced Wall Treatment
KH, RT	Kelvin-Helmholtz, Rayleigh-Taylor
LES	Large-Eddy Simulation
LMR	Local Momentum Ratio
LPT	Lagrangian Particle Tracking
PE	Pilch-Erdman
(U)RANS	(Unsteady) Reynolds-Averaged Navier-Stokes
VOF	Volume of Fluid
SMD	Sauter Mean Diameter

Among the various pintle injector architectures, the discrete-orifice configuration with circular holes represents a widely adopted solution for liquid propellant systems [3,7,13]. In this design, the radial propellant stream exits through multiple circular orifices distributed along the pintle circumference, producing discrete jets that impinge on the surrounding annular flow. The atomization mechanism in circular discrete-orifice injectors is governed by column-type breakup, where the liquid jet disintegrates under the combined action of aerodynamic shear, Kelvin-Helmholtz and Rayleigh-Taylor instabilities, and turbulent fluctuations originating within the orifice passage [14,15]. The resulting spray characteristics, including droplet size distribution, spatial dispersion, velocity field, and penetration depth, are strongly dependent on the orifice geometry, injection pressure differential, and the properties of the surrounding gas environment.

Computational Fluid Dynamics (CFD) has become a fundamental tool for investigating liquid–gas interactions in rocket injectors, enabling detailed analysis of atomization, mixing, and combustion without the cost and complexity of full-scale experimental campaigns. Two principal numerical strategies are employed to simulate atomization phenomena: interface-resolving methods and Lagrangian-based formulations. In the first category, the Volume of Fluid (VOF) model [16] and related Eulerian techniques allow for direct tracking of the gas–liquid interface, enabling accurate representation of the early deformation and primary breakup of liquid jets and sheets [17]. However, these methods require extremely fine computational grids, adaptive mesh refinement techniques, and small time steps to fully resolve the interface dynamics, resulting in substantial computational costs that limit their applicability to short physical times and small spatial domains.

In the Lagrangian framework, the dispersed phase is represented as a collection of computational parcels, each encompassing a statistical ensemble of droplets sharing identical physical properties. This approach is referred to as the Discrete Phase Model (DPM) in the context of ANSYS Fluent [18] and as Lagrangian Particle Tracking (LPT) in OpenFOAM [19] and the broader academic literature. The core idea is to track individual parcel trajectories within an Eulerian carrier-phase flow field and is particularly suited for modeling secondary breakup, evaporation, and spray dispersion over extended domains at manageable computational cost [20]. Hybrid strategies such as VOF-to-DPM transition and VOF–LPT coupling [8,17,21,22] have emerged as high-fidelity approaches that combine the accuracy of interface resolving methods in the primary breakup region with the computational efficiency of Lagrangian tracking for downstream spray evolution. These methodologies capture the detailed physics of jet disintegration near the injector exit and seamlessly transition to a dispersed-phase representation once

the liquid core fragments into discrete droplets. Shi et al. [21] simulated the atomization process of a radial orifice–type gas–liquid pintle element under periodic operating conditions using VOF-to-DPM. Zhang et al. [23] applied the technique on circular orifice pintle injectors with a good agreement in the spray penetration and Sauter Mean Diameter (SMD) prediction in comparison to experimental data. Nevertheless, even hybrid VOF–Lagrangian formulations remain computationally demanding, particularly when applied to full injector geometries or when extensive parametric investigations are required, motivating the continued development of purely Lagrangian approaches with physically grounded initial conditions.

A critical challenge in purely Lagrangian spray modeling lies in the specification of initial conditions for the dispersed phase, since no interface-resolving method is employed to describe primary breakup. Two principal strategies have been established in the literature: prescribed droplet size distributions and blob injection. The former imposes a statistical representation of the post-atomization droplet population directly at the injector exit, most commonly through a Rosin-Rammler distribution [14] parameterized against experimental data or atomization correlations, and is used when downstream spray statistics are available for calibration. In contrast, the blob injection concept, introduced by Reitz [24], replaces the intact liquid core emerging from the nozzle with a stream of spherical computational parcels termed blobs, whose initial diameter equals the nozzle orifice diameter. The liquid jet exit condition is thus represented as a succession of large, nozzle-sized droplets, and the entire atomization cascade is delegated to secondary breakup models acting along the parcel trajectory downstream of injection. Blob injection requires no characterization of the primary breakup region and is compatible with any secondary breakup model. More importantly, it provides a physically motivated initial condition: the unbroken liquid column exiting the nozzle undergoes progressive surface stripping downstream, a sequence consistent with the observed mechanism of turbulent jet atomization [24,25]. Its principal limitation is that spray predictions are sensitive to the accuracy and calibration of the secondary breakup model, which must reproduce the entire atomization history from nozzle exit to the fully dispersed spray.

Compared with a prescribed size distribution, blob injection also avoids a methodological circularity: imposing the post-atomization droplet population directly at the injector exit either presupposes the very spray statistics that the simulation aims to predict. Blob injection instead initializes the dispersed phase with the only unambiguous physical condition available at the orifice, i.e. the intact liquid column at nozzle diameter, and lets the secondary breakup model reconstruct the atomization history along the parcel trajectory. In this sense, it can be regarded as the natural Lagrangian counterpart of the interface-resolving initialization employed in VOF approaches.

Regarding the breakup models, different ones have been introduced over the years. One of the earliest formulation widely adopted in Lagrangian frameworks is the Taylor Analogy Breakup (TAB) model [26], which treats droplet oscillation as a forced spring-mass-damper system and predicts breakup once the deformation exceeds a critical threshold; its range of applicability is generally restricted to low Weber number conditions. The Wave model [24], derived from a Kelvin-Helmholtz (KH) instability analysis of the cylindrical liquid-gas interface, predicts the continuous shedding of small child droplets from a parent parcel at a rate set by the fastest-growing surface wave. The model introduces a breakup constant B_1 controlling the breakup time scale, which is known to vary with operating conditions and injector geometry [27,28]. The KH-RT model [25] supplements the surface-stripping mechanism with a Rayleigh-Taylor (RT) instability criterion; this combined formulation has become the dominant choice for high-speed diesel-like sprays [29,30], at the cost of additional empirical constants, whose values remain problem-dependent. The Reitz-Diwakar model [31] takes a regime-classification approach, distinguishing bag and stripping breakup on the basis of local conditions and liquid properties, and prescribing empirical correlations for child droplet sizes. The Pilch-Erdman (PE) model [32] maps the full set of breakup regimes to experimentally derived correlations for child droplet sizes and breakup completion time through a dimensionless breakup time, without requiring user-specified calibration constants, which is a practical advantage in configurations where reference data are unavailable.

A further limitation of blob injection concerns the aerodynamic representation of the unresolved liquid column. In the native Madabhushi formulation, the column is carried by spherical blobs and a constant column-phase drag coefficient is imposed until the column-breakup time [18,33]. The real column, however, bends and deforms while its projected area, pressure distribution and wake evolve. Numerical studies of deformable droplets and high-Weber-number liquid columns show that these effects can produce substantial and non-steady variations of the aerodynamic drag [34–36]. A fixed spherical-blob closure may therefore under-represent the effective aerodynamic loading during portions of the pre-breakup history, although the sign and magnitude of this discrepancy are not universal.

Drag and breakup cannot generally be treated as independent closures in a Lagrangian spray calculation. Liu et al. [37] showed that changes in the drag formulation can modify the predicted Sauter mean diameter through their interaction with breakup and coalescence. In the Madabhushi framework, the column drag acts only before the column-breakup time, while the downstream population results from Wave stripping, Pilch-Erdman fragmentation, transport and parcel interactions [18,33]. The influence of a column-phase correction on downstream diameters must therefore be established from the spatially resolved spray response and cannot be inferred from the drag force alone.

The Madabhushi model [33] uses the blob injection and the combination of two breakup mechanisms in a sequential, physically motivated structure. During an initial column breakup phase, the parent parcel undergoes surface stripping governed by KH wave instability, acting as a surrogate for primary atomization of the liquid core. Once the column breakup time is exceeded, the remaining liquid mass is treated as fully fragmented and the Pilch-Erdman model is applied to determine the child droplet population, inheriting its freedom from calibration constants for this terminal step. This two-stage structure directly maps onto the physical sequence implied by blob injection: the Wave phase [24] reproduces the progressive stripping of the unbroken liquid column, while the PE step provides the secondary droplet sizes without additional tuning. A further reason for this choice is that, unlike the Wave and KH-RT formulations, whose constants are commonly tuned for high-pressure diesel-like sprays injected along the gas stream, the Madabhushi model was formulated specifically for the breakup of a liquid jet in gaseous crossflow [33], which is precisely the configuration of the discrete-orifice pintle injector considered here. For this reason, the Madabhushi model is adopted in the present work as the secondary breakup model associated with blob injection.

Alongside the choice of the breakup model, turbulence modeling plays a critical role in spray simulations, as turbulent fluctuations influence interface instabilities, droplet breakup, and dispersion [38]. Available frameworks span a wide range of fidelity and cost [39]: Direct Numerical Simulation (DNS) resolves all scales of motion but remains confined to low-Reynolds-number academic configurations; Large-Eddy Simulation (LES) resolves the energy-containing eddies and captures unsteady atomization dynamics with high fidelity, at a computational cost that generally precludes its use in parametric or design-oriented studies; hybrid RANS-LES formulations such as Detached-Eddy Simulation (DES) offer an intermediate trade-off [40]. Unsteady Reynolds-Averaged Navier-Stokes (URANS) formulations, in contrast, solve the time-dependent ensemble-averaged flow equations while modeling the full spectrum of turbulent fluctuations, thereby offering a substantially more tractable framework for complex geometries and broad operating-condition surveys [39].

Despite this computational advantage, the predictive scope of URANS-based Euler-Lagrange approaches is inherently narrower than that of scale-resolving, interface-capturing methods. Because URANS

advances the time-dependent ensemble-averaged carrier-phase equations, the turbulent fluctuations, intermittency, and three-dimensional coherent structures responsible for the large-scale unsteadiness of the column-bending region are modeled rather than explicitly resolved, resulting in an expected loss of fidelity relative to LES for instantaneous and higher-order flow quantities [41]. Moreover, in a parcel-based Euler-Lagrange formulation, the continuous liquid interface is not directly tracked; consequently, the instantaneous deformation of the liquid column and the formation and breakup of sheets and ligaments are represented through phenomenological injection and breakup models rather than explicitly reconstructed [42]. Such a framework is therefore intended primarily for the prediction of time-averaged and integral spray characteristics, such as mean trajectory and penetration, breakup location, droplet-size and velocity statistics, and overall dispersion patterns, within the range of operating conditions for which the adopted closures are calibrated or validated. It is not intended to reproduce the instantaneous three-dimensional topology and unsteady dynamics of the primary-atomization process.

In this paper, a URANS Euler-Lagrange methodology is proposed for circular discrete-orifice pintle injectors operating in gaseous crossflow, based on blob injection coupled with the Madabhushi secondary breakup model. The approach requires no interface-resolving treatment of the primary atomization region, and the sequential wave-shedding and Pilch-Erdman fragmentation steps of the Madabhushi model provide a physically consistent description of the primary-to-secondary breakup transition directly compatible with the blob injection paradigm. Model constants are determined from literature data for plain-orifice liquid jets in gaseous crossflow at Weber numbers and liquid-to-gas density ratios representative of the present operating conditions.

The proposed methodology is validated against four test cases. Two cases rely on experimental measurements and assess the capability of the proposed approach to reproduce observed spray characteristics under well-documented operating conditions. The other two cases are numerical reference solutions drawn from high-fidelity LES VOF-to-DPM simulations available in the literature [8], which explicitly resolve the liquid core dynamics and the early fragmentation region. These LES VOF-to-DPM solutions serve as a scale-resolving benchmark against which the fully Lagrangian URANS methodology is assessed, enabling a quantitative evaluation in terms of droplet size distributions, velocity profiles and spatial spray patterns. The comparison between the two frameworks clarifies both the predictive reach and the inherent limitations of the proposed approach within the constraints of a URANS formulation.

The contribution of the present work is threefold: (i) a set of breakup constants determined a priori from literature values and correlations, with the column-breakup constant evaluated as a function of the operating condition rather than tuned, which reduces the calibration uncertainty; (ii) a preliminary effective projected-area closure for the column-phase drag, bounded through a dedicated sensitivity assessment of the spatially resolved diameter profiles; and (iii) a systematic application of the blob-injection Madabhushi framework to the circular discrete-orifice gas-liquid pintle configuration, validated against both experimental measurements and LES VOF-to-DPM reference data.

This work is structured as follows. Section 2 introduces the governing Euler–Lagrange equations and the associated sub models for droplet dynamics, drag, coalescence, and breakup. Section 3 presents the test case configurations and the corresponding numerical setup. Section 4 explains the numerical data processing methods. Section 5 discusses the simulation results and their comparison with experimental and LES VOF-to-DPM data. Finally, Section 6 summarizes the main findings.

2. Numerical modeling

2.1. Gas phase equations

The unsteady compressible Reynolds-Averaged Navier-Stokes (URANS) equations in conservative form govern mass and momentum transport of the Eulerian phase. The continuity equation can be expressed as:

$$\frac{\partial \rho}{\partial t} + \nabla \cdot (\rho \vec{v}) = S_m \tag{1}$$

where ρ is the density, $\vec{v}$ is the velocity vector and S_m is the source term. The momentum equation is:

$$\frac{\partial (\rho \vec{v})}{\partial t} + \nabla \cdot (\rho \vec{v}\vec{v}) = -\nabla p + \nabla \cdot (\bar{\bar{\tau}}) + \rho \vec{g} + \vec{F} \tag{2}$$

where $\vec{g}$ is the gravitational acceleration, $\vec{F}$ is the vector of external forces, and the viscous stress tensor for Newtonian fluids is:

$$\bar{\bar{\tau}}_{\text{eff}} = \mu \left[(\nabla \vec{v} + \nabla \vec{v}^T) - \frac{2}{3} (\nabla \cdot \vec{v}) I \right] - \frac{2}{3} \rho k I \tag{3}$$

Here, μ is the effective viscosity, accounting for molecular and turbulent viscosity, k is the turbulent kinetic energy, and I is the identity tensor. The energy equation is:

$$\frac{\partial}{\partial t} \left(\rho \left(e + \frac{v^2}{2} \right) \right) + \nabla \cdot \left(\rho \vec{v} \left(h + \frac{v^2}{2} \right) \right) = \nabla \cdot \left(k_{\text{eff}} \nabla T + (\bar{\bar{\tau}}_{\text{eff}} \cdot \vec{v}) \right) + S_h \tag{4}$$

where e is the internal energy, h is the enthalpy, k_{eff} is the effective conductivity accounting also for turbulent thermal conductivity and S_h is the energy source term. The energy equation is retained for completeness of the compressible-flow description; under the present cold-flow conditions no evaporation occurs, so that no interphase mass-transfer source is active and the dispersed-phase heat transfer does not modify the droplet size, while S_h accounts only for the thermal two-way coupling with the parcels.

2.2. Lagrangian equations

The motion of a discrete-phase particle is determined by solving the instantaneous force balance in a Lagrangian framework [18]:

$$m_p \frac{\mathrm{d}\vec{u}_p}{\mathrm{d}t} = m_p \frac{\vec{v} - \vec{u}_p}{\tau_r} + m_p \frac{\vec{g}(\rho_p - \rho)}{\rho_p} + \vec{F}_e \tag{5}$$

where m_p and $\vec{u}_p$ denote the particle mass and velocity, $\vec{v}$ is the local gas velocity, $\vec{g}$ is the gravitational acceleration, ρ_p and ρ are the particle and gas densities, and $\vec{F}_e$ collects any additional external forces like virtual mass force or thermophoretic effects. The first term on the right-hand side is the drag force, expressed through the relaxation time:

$$\tau_r = \frac{\rho_p d_p^2}{18\mu} \frac{24}{C_d Re} \tag{6}$$

where d_p is the particle diameter, μ is the gas dynamic viscosity, and C_d is the drag coefficient evaluated at the particle Reynolds number $Re = \rho d_p |\vec{u}_p - \vec{v}| / \mu$. The second term accounts for buoyancy-corrected gravity. By integrating Eq. (5) over time, the instantaneous particle velocity is obtained; the position is subsequently updated through the kinematic relation:

$$\frac{\mathrm{d}\vec{x}}{\mathrm{d}t} = \vec{u}_p \tag{7}$$

Translational motion is coupled with particle rotation through the angular momentum balance:

$$I_p \frac{\mathrm{d}\vec{\omega}_p}{\mathrm{d}t} = \frac{\rho}{2} \left(\frac{d_p}{2} \right)^5 C_\omega |\vec{\Omega}| \cdot \vec{\Omega} \tag{8}$$

where I_p is the moment of inertia of the particle, $\vec{\omega}_p$ is the particle angular velocity, and $\vec{\Omega} = \frac{1}{2} \nabla \times \vec{v} - \vec{\omega}_p$ is the relative angular velocity. The rotational drag coefficient C_ω follows the Dennis et al. correlation [43]:

$$C_\omega = \frac{6.45}{\sqrt{Re_\omega}} + \frac{32.1}{Re_\omega} \tag{9}$$

with the rotational Reynolds number $Re_\omega = \rho |\vec{\Omega}| d_p^2 / (4\mu)$. The rotational balance is included for completeness of the force description.

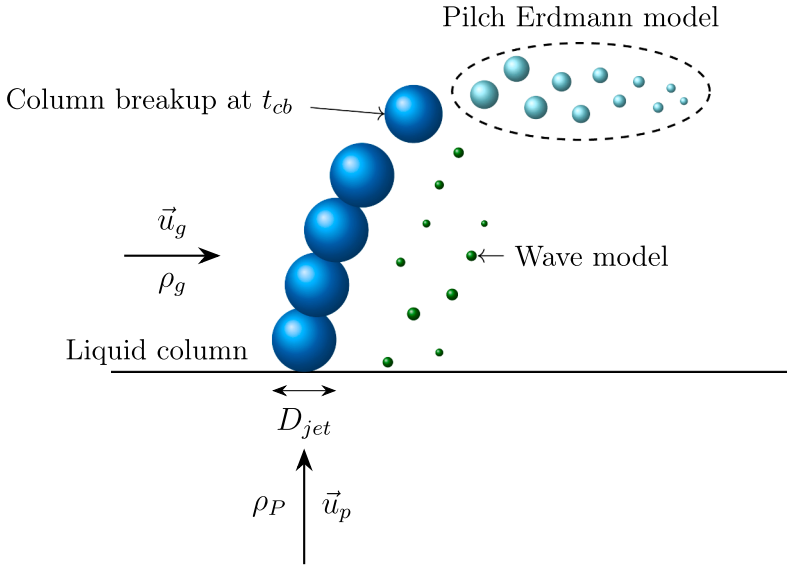


Fig. 1. Schematic representation of the Madabhushi breakup model. Adapted from Fluent manual [18].

2.3. Breakup and drag models

As discussed in the introduction, the accurate modeling of secondary breakup is central to the predictive capability of the Lagrangian framework. The drag force constitutes an equally critical mechanism, as it governs the momentum exchange between the dispersed particles and the surrounding gas phase and therefore directly influences particle trajectories, penetration, and dispersion throughout the flow field.

In this work, the secondary breakup is modeled using the approach proposed by Madabhushi [33], which is implemented through a blob injection strategy. This injection method is central to the present framework, as it initializes the spray as a discrete population of liquid blobs with a diameter equal to the nozzle exit. The Madabhushi model integrates the Kelvin-Helmholtz (KH) instability mechanism for the column breakup phase with the Pilch-Erdman correlation [32] for the subsequent secondary fragmentation. By utilizing the blob injection approach, the model characterizes the morphological evolution and size distribution of the particles resulting from aerodynamic instabilities. In this framework, the Kelvin-Helmholtz and Rayleigh-Taylor instabilities are not additional user-selected options but the physical mechanisms underlying aerodynamic secondary breakup: the former drives the shear stripping of the liquid column, while the latter governs the fragmentation of the accelerating, deforming droplet. A schematic representation of the Madabhushi model is provided in Fig. 1.

Liquid column phase. In the primary breakup stage, the liquid jet is represented as a column of spherical particles with initial diameter D_0. During this phase, child particles are shed from the liquid column according to the Wave model [24], which assumes that the breakup time and the resulting particle size are related to the fastest-growing Kelvin-Helmholtz instability arising from aerodynamic shear at the liquid-gas interface. The wavelength Λ and growth rate Ω of this instability are correlated as functions of the local dimensionless groups through the expressions reported by Reitz [24]:

$$\frac{\Lambda}{a} = \frac{9.02\,(1+0.45\,\mathrm{Oh}^{0.5})(1+0.4\,\mathrm{Ta}^{0.7})}{(1+0.87\,\mathrm{We}_g^{1.67})^{0.6}} \tag{10}$$

$$\Omega\sqrt{\frac{\rho_l\,a^3}{\sigma}} = \frac{0.34+0.38\,\mathrm{We}_g^{1.5}}{(1+\mathrm{Oh})(1+1.4\,\mathrm{Ta}^{0.6})} \tag{11}$$

where a is the parent parcel radius, σ is the liquid-gas surface tension, and the relative velocity magnitude is defined as $u_{rel} = |\vec{v} - \vec{u}_p|$. The relevant dimensionless groups are defined as:

$$\mathrm{We}_g = \frac{\rho\,u_{rel}^2\,a}{\sigma}, \qquad \mathrm{We}_l = \frac{\rho_l\,u_{rel}^2\,a}{\sigma} \tag{12}$$

$$\mathrm{Re}_l = \frac{u_{rel}\,a}{\nu_l}, \qquad \mathrm{Oh} = \frac{\sqrt{\mathrm{We}_l}}{\mathrm{Re}_l}, \qquad \mathrm{Ta} = \mathrm{Oh}\sqrt{\mathrm{We}_g} \tag{13}$$

with $\vec{v}$ and $\vec{u}_p$ denoting the fluid and particle velocity vectors, ν_l the liquid kinematic viscosity, We_g and We_l the gas and liquid phase Weber numbers, Re_l the liquid Reynolds number, Oh the Ohnesorge number, and Ta the Taylor number. The radius of the child particles is assumed proportional to the wavelength of the fastest-growing surface wave:

$$r = B_0\,\Lambda \tag{14}$$

where B_0 is a calibration constant and Λ is calculated from Eq. (10). The parent parcel radius evolves as $\mathrm{d}a/\mathrm{d}t = -(a-r)/\tau$, with the breakup time τ given by:

$$\tau = \frac{3.726\,B_1\,a}{\Lambda\,\Omega} \tag{15}$$

The liquid column undergoes breakup once the elapsed time exceeds $t_{cb} = C_0\,(D_0/|\vec{v}|)\sqrt{\rho_l/\rho_g}$.

In this phase, moreover, the liquid column drag is assumed to be constant.

Secondary breakup phase. Once the particle lifetime exceeds t_{cb}, secondary breakup occurs according to the Pilch–Erdman model [32]. The particle undergoes deformation within a characteristic period $t_{def} = 1.6\,t^*$, where the breakup timescale is:

$$t^* = \frac{D_{cb}}{u_{rel}}\sqrt{\frac{\rho_l}{\rho}} \tag{16}$$

where D_{cb} is the local droplet diameter at the column breakup point. During deformation time t_{def}, the drag coefficient transitions linearly from a spherical particle drag to a disk particle drag $C_D^{disk} = 1.2$:

$$C_D = C_D^{sphere}\left(1 - \frac{t}{t_{def}}\right) + C_D^{disk}\,\frac{t}{t_{def}}, \qquad t < t_{def} \tag{17}$$

The aerodynamic drag force acting on the deforming droplet is:

$$F_D = \frac{1}{2}\,\rho_g\,C_D\,A_p'\,\left|\vec{u}_g - \vec{u}_p\right|\left(\vec{u}_g - \vec{u}_p\right) \tag{18}$$

where the effective cross-sectional area A_p' accounts for the droplet deformation through a reference diameter D_{ref} calculated from the Weber number and t_{def}:

$$A_p' = \frac{\pi}{4} D_{ref}^2 = \frac{D_{ref}^2}{D_{cb}^2} \frac{\pi}{4} D_{cb}^2 = \left(\frac{D_{ref}}{D_{cb}} \right)^2 A_p^{cb} \tag{19}$$

where A_p^{cb} is the value at column breakup. Once the deformation time t_{def} is reached, the droplet remains fully deformed and the drag stays constant at C_D^{disk}, with reference diameter:

$$D_{ref} = \begin{cases} \left(1 + 0.19\sqrt{\mathrm{We}}\right) D_{cb} & We < 100 \\ 2.9\, D_{cb} & We \geq 100 \end{cases} \tag{20}$$

until the droplet breaks up into five smaller child droplet parcels. The total breakup time t_b depends on the local Weber number and is computed through regime-dependent correlations that account for bag, multimode, and shear breakup mechanisms:

$$\frac{t_b}{t^*} = \begin{cases} 6\,(\mathrm{We} - 12)^{-0.25}, & 12 < \mathrm{We} < 18 \\ 2.45\,(\mathrm{We} - 12)^{0.25}, & 18 < \mathrm{We} < 45 \\ 14.1\,(\mathrm{We} - 12)^{-0.25}, & 45 < \mathrm{We} < 351 \\ 0.776\,(\mathrm{We} - 12)^{0.25}, & 351 < \mathrm{We} < 2670 \\ 5.5, & 2670 < \mathrm{We} \end{cases} \tag{21}$$

Due to rim expansion, the velocity of each child droplet $\vec{u}_{child}$ is calculated as:

$$\vec{u}_{child} = \vec{u}_{parent} + \vec{u}_n \tag{22}$$

where $\vec{u}_{parent}$ is the parent droplet velocity, and $\vec{u}_n$ is a normal velocity component in a plane perpendicular to the parent droplet velocity, with magnitude:

$$u_n = 5 \frac{D_{parent}}{t_b - t_{def}} \tag{23}$$

For each of the five droplets, the normal velocity direction angle α is randomly chosen in the range $[0, 2\pi]$, ensuring physically realistic dispersion of the spray.

The child droplet diameters follow a root-normal distribution:

$$f(D_{child}) = \frac{\sqrt{\frac{D_{child}}{D_{0.5}}}}{2\sqrt{2\pi} \cdot 0.238 \cdot D_{child}} \exp\left(-\frac{1}{2} \left(\frac{\sqrt{\frac{D_{child}}{D_{0.5}}} - 1}{0.238} \right)^2 \right) \tag{24}$$

where $D_{0.5} = 1.2 D_{SMD}$ is the mass median diameter, related to the target Sauter Mean Diameter after breakup:

$$D_{SMD} = 1.5 \frac{Oh^{0.2}}{We_{corr}^{0.25}} D_{parent} \tag{25}$$

Here, Oh is the Ohnesorge number based on the reference diameter:

$$\mathrm{Oh} = \frac{\mu_l}{\sqrt{\rho_l \sigma D_{ref}}} \tag{26}$$

The corrected Weber number We_{corr} accounts for viscous effects at high Ohnesorge numbers ($\mathrm{Oh} > 0.1$):

$$\mathrm{We}_{corr} = \frac{\mathrm{We}}{1 + 1.077\,\mathrm{Oh}^{1.6}} \tag{27}$$

To improve the morphological representation of the fragmentation process, the correction proposed by Lambert et al. [44] is used for the secondary breakup phase. The particles undergoing secondary breakup immediately following the column breakup stage represent physical ligaments detaching from the liquid core. Since these ligaments exhibit non-spherical geometries, the standard Pilch and Erdman model tends to overestimate the resulting child particle diameters in this specific region. To account for this effect, the diameters of the child particles produced during the initial secondary breakup event after column breakup are weighted by a factor $F_{Lig} > 0$:

$$D_{child} = F_{Lig} \bar{D}_{child} \tag{28}$$

where $\bar{D}_{child}$ follows the distribution defined in Eq. (24). For all subsequent fragmentation events, the weighting factor is set to $F_{Lig} = 1$ until surface tension forces stabilize the particles against further breakup. Furthermore, the child particles shed from the liquid core via the Wave model during the primary breakup phase are also subjected to the Pilch-Erdman secondary breakup mechanism once they detach from the parent parcel, ensuring a unified treatment of the dispersed phase.

2.4. Turbulence modeling

The URANS equations are solved in together with the Realizable k-ϵ turbulence model [45]. To ensure an accurate representation of the boundary layer and near-wall physics, the Enhanced Wall Treatment (EWT) is adopted, which combines a blended law-of-the-wall approach with a two-layer model to resolve the viscous sublayer when the mesh is sufficiently refined ($y^+ \approx 1$).

The selection of the Realizable k-ϵ model is motivated by its generally better performance over the standard k-ϵ formulation in flows involving high curvature, rotation, and secondary flow features typical of crossflow injection [45–47]. Specifically, the realizability constraint, which ensures non-negative normal stresses and consistency with Schwarz's inequality, allows for more accurate predictions of the spreading rate of both planar and round jets [18].

2.5. Other submodels

Turbulent dispersion is modeled with a stochastic Lagrangian approach using the Discrete Random Walk (DRW) model. Two-way coupling with turbulence is included via a sink term in the turbulent kinetic energy equation [48]. Droplet collisions are treated with the stochastic O'Rourke model [49], allowing for coalescence or bouncing depending on particle dynamics and flow conditions. To mitigate the point-source stiffness of the two-way coupling in the dense near-orifice region, where the dilute assumptions of the discrete-phase and collision models are most strained, the dispersed-phase source terms are distributed onto the Eulerian mesh through a node-based Gaussian kernel.

3. Computational setup

3.1. Test cases description

As stated in the Introduction, the objective of this paper is to introduce a physics-based Lagrangian injection model and to assess its predictive capabilities by comparison with hybrid VOF-Lagrangian approaches (e.g., VOF-to-DPM) and experimental measurements.

3.1.1. Experimental test cases

The first test case, based on the experimental work of Zhang et al. [50], is used to assess the capability of the model to reproduce observed spray characteristics at different operating pressures. The injector features a pintle tip of diameter $D_p = 13.2$ mm, through which liquid water is supplied via eight radial holes of diameter 0.6 mm, while air is delivered through an axial annular gap of width $H = 0.4$ mm surrounding a liquid channel of diameter $D_c = 8$ mm. Experiments were conducted inside an ambient-pressure chamber equipped with quartz glass optical windows, and droplet size data were acquired using a Spraylink High-speed Spray Particle Size Analyzer (SHSSPSA), providing Sauter Mean Diameter (SMD) measurements at various spatial locations across seven operating conditions spanning a range of chamber pressures and liquid

Table 1
Test cases for validation.

Test case	Ref.	Condition
TC1-P1	[50]	$p_a = 0.5$ MPa
TC1-P2		$p_a = 0.6$ MPa
TC2-W1	[8]	$We_g = 3500$
TC2-W2		$We_g = 8500$

and gas mass flow rates. The SMD, or D_{32}, is one of the most used diameter in combustion, mass transfer, and efficiency studies, and is defined as the diameter of the drop whose ratio of volume to surface area is the same as that of the entire spray [14]:

$$\text{SMD} = D_{32} = \frac{\sum_i N_i D_i^3}{\sum_i N_i D_i^2} \tag{29}$$

where i is the size range considered, N_i is the number of drops in size range i, and D_i is the middle diameter of size range i.

3.1.2. Numerical test cases

The second case, derived from the study by Zhang et al. [8], provides a comparative basis against a LES VOF-to-DPM simulation of a Gas-film/Liquid-jet On Pintle (GLOP) injection element. The configuration consists of a gas film region of height $W = 8$ mm and length $L = 32$ mm, with a circular liquid jet orifice of diameter $d = 1.6$ mm and a jump distance between the gas film exit and the jet centerline of $L_s = 15$ mm; nitrogen and water are used as the gas and liquid phases, respectively. This configuration is used to evaluate the model across different gas Weber numbers while maintaining a constant Local Momentum Ratio (LMR ≈ 1), and quantitative validation is performed against SMD measurements, droplet velocity profiles, arithmetic mean diameter D_{10}, and size distribution statistics at 60 mm downstream of the injector.

The mean diameter D_{10} is defined as [14]:

$$D_{10} = \frac{\sum_i N_i D_i}{\sum_i N_i} \tag{30}$$

while the LMR is defined as the ratio of the momentum flux of a single radial jet to that of the axial gas flow intercepted over the projected area of one orifice:

$$\text{LMR} = \frac{\dot{m}_l v_l}{\dot{m}_g v_g} \Big/ \left(\frac{d}{L}\right) \tag{31}$$

where $\dot{m}$ and v are respectively the mass flow rates and the velocities, subscripts l and g are liquid and gas phases, d is the orifice diameter and L is the gas film length. In discrete-orifice pintle injector configurations, key spray characteristics such as jet penetration angle and SMD are governed by this local quantity rather than by the total integrated momentum ratio of the two streams.

The test cases are finally detailed in Table 1. In the following, p_a denotes the ambient pressure while We_g the gas Weber number.

3.2. Computational domains and boundary conditions

Computational domains have been constructed to reproduce the experimental and numerical setups of the respective test cases. For TC1, a half-domain (4 injection holes) is simulated with a symmetry boundary condition at the midplane, given the geometric symmetry of the experimental apparatus domain. For TC2, the computational domain reproduces a pintle injector element, defined as the minimal representative unit of the full injector comprising a single radial orifice and the corresponding portion of the axial gas film, enclosed in a rectangular domain with symmetry conditions applied in the lateral directions. These reduced domains reproduce the same symmetry setup adopted in the corresponding reference configurations; simulating a single representative element with lateral symmetry, rather than the full set of discrete jets, is a standard practice for periodic injector arrays [8,13].

Table 2
Boundary conditions and setup types for the TC1 and TC2 test cases.

Case	Type	Parameters
TC1-P1	Mass Flow Inlet	$p = .5$ MPa, $\dot{m} = 0.00555$ kg/s
	Pressure Outlet	$p = .5$ MPa
TC1-P2	Mass Flow Inlet	$p = .6$ MPa, $\dot{m} = 0.00555$ kg/s
	Pressure Outlet	$p = .6$ MPa
TC2-W1	Velocity Inlet	$p = 1$ atm, $u = 163.1$ m/s
	Pressure Outlet	$p = 1$ atm
TC2-W2	Velocity Inlet	$p = 1$ atm, $u = 257.6$ m/s
	Pressure Outlet	$p = 1$ atm
All Cases	Sides of the domain	Symmetry
	Wall	No-slip, adiabatic Wall

Table 3
Grid convergence: relative deviation of each case from the baseline solution, $\varepsilon_\phi = (\phi - \phi_{\text{base}})/\phi_{\text{base}}$, at the $x = 60$ mm downstream sampling plane, $We_g = 8500$.

Quantity	Baseline	ε_ϕ - Fine grid	ε_ϕ - Coarse grid
d_{10}	24.57	+4.40%	−2.44%
d_{50}	50.11	+3.39%	−0.03%
d_{90}	80.33	+1.41%	−18.84%
D_{32}	77.52	−1.10%	−20.62%

A common meshing strategy is adopted for both test cases. The grid is designed to yield $y^+ \approx 1$ under the lowest bulk velocity conditions for TC1 and TC2. As the velocity increases, the wall shear stress rises, leading to an increase in the local y^+ value for a fixed mesh spacing. To ensure accuracy across all regimes, this strategy is coupled with the Enhanced Wall Treatment (EWT) of the Realizable k-ϵ model. EWT allows the solver to resolve the viscous sublayer when $y^+ \approx 1$ and automatically switches to wall functions if the first grid cell falls into the log-law region at higher Reynolds numbers. A local refinement box is applied in the injection region to capture the near-field spray dynamics, following the standard procedures in spray simulations [51]. The specific boundary conditions for each test case are detailed in Table 2.

3.3. Convergence study

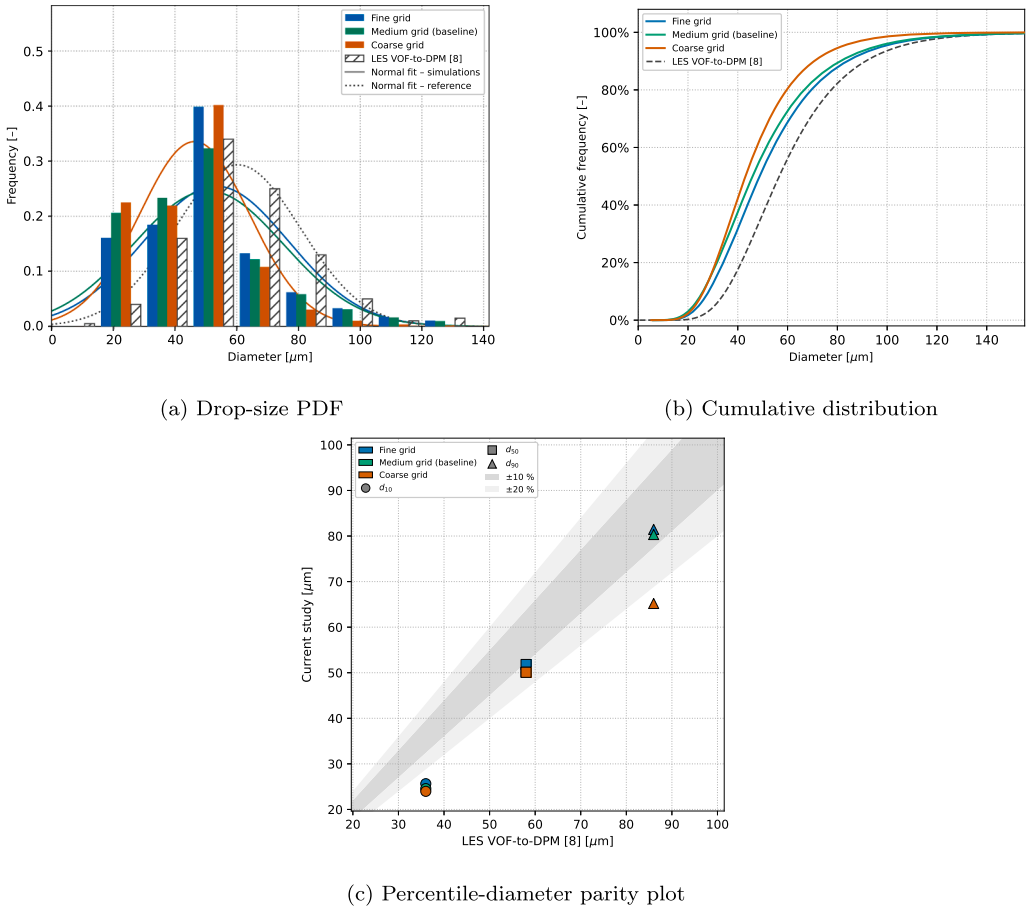
A systematic convergence study was conducted to ensure that the numerical results are independent of both spatial and temporal discretization, following the procedure of Radhakrishnan et al. [52].

The spatial resolution was evaluated on the most restrictive operating condition among the TC1 and TC2 testcases, identified as the configuration with the highest injection velocities, at a fixed time step of $\Delta t = 10^{-5}$ s.

Three mesh levels (coarse, medium, and fine) characterized by progressively smaller cell sizes in the near-injection refinement region were tested. The spatially converged grid was identified based on the stabilization of the Sauter Mean Diameter at selected downstream locations and the spray penetration, and adopted for all subsequent simulations.

Temporal convergence was then assessed independently for each test case on the converged grid, by varying the time step until the spray penetration and the spatial evolution of the SMD reached a stable solution.

The results of the grid-refinement study (coarse 966518, medium 1802263, fine 5,509,239 cells, respectively) for the case $We_g = 8500$ are summarized in Table 3, which reports the relative deviation of each spray metric from the medium (baseline) grid. Refining the medium grid to the fine level changes the Sauter Mean Diameter by only −1.1% and the d_{90} percentile by +1.4%, while the median diameter d_{50} varies by +3.4%; the medium grid is therefore within the asymptotic range for the diameter statistics and is retained as the converged spatial discretization. Coarsening the grid, on the contrary, produces much larger deviations, exceeding 18% in magnitude on both D_{32} and d_{90}: as confirmed



(a) Drop-size PDF

(b) Cumulative distribution

(c) Percentile-diameter parity plot

Fig. 2. Grid convergence at $We_g = 8500$: (a) drop-size probability density function, (b) cumulative distribution, and (c) parity of the percentile diameters, for the coarse, medium (baseline) and fine grids compared with the LES VOF-to-DPM reference.

Table 4
Time-step convergence: relative deviation of each case from the baseline solution, $\epsilon_\phi = (\phi - \phi_{base})/\phi_{base}$, at the $x = 60$ mm downstream sampling plane, $We_g = 8500$.

Quantity	Baseline	ϵ_ϕ - $\Delta t = 1.0 \times 10^{-6}$ s	ϵ_ϕ - $\Delta t = 5.0 \times 10^{-6}$ s
d_{10}	24.57	−2.95%	+3.69%
d_{50}	50.11	−3.75%	+2.41%
d_{90}	80.33	−2.45%	−1.07%
D_{32}	77.52	+1.03%	+0.10%

Table 5
Final temporal discretization settings for each test case following the convergence study.

Case	Cells no.	Time-step Δt [s]
TC1-P1	2098706	5×10^{-6}
TC1-P2		5×10^{-6}
TC2-W1	1802263	5×10^{-6}
TC2-W2		2.5×10^{-6}

by the drop-size distributions in Fig. 2, the coarse grid over-populates the intermediate-diameter range and truncates the large-droplet tail, so that its apparently closer D_{32} agreement with the reference is spurious and merely reflects the loss of the largest droplets.

The time-step study, reported in Table 4, shows that the diameter statistics are essentially insensitive to the temporal resolution: between $\Delta t = 1.0 \times 10^{-6}$ s and 5.0×10^{-6} s the Sauter Mean Diameter varies by at most 1.0% and all diameter percentiles by less than 3.8% with respect to the 2.5×10^{-6} s baseline, and the drop-size distributions overlap almost exactly (Fig. 3).

The time steps adopted for each configuration and the final grid cell numbers are summarized in Table 5.

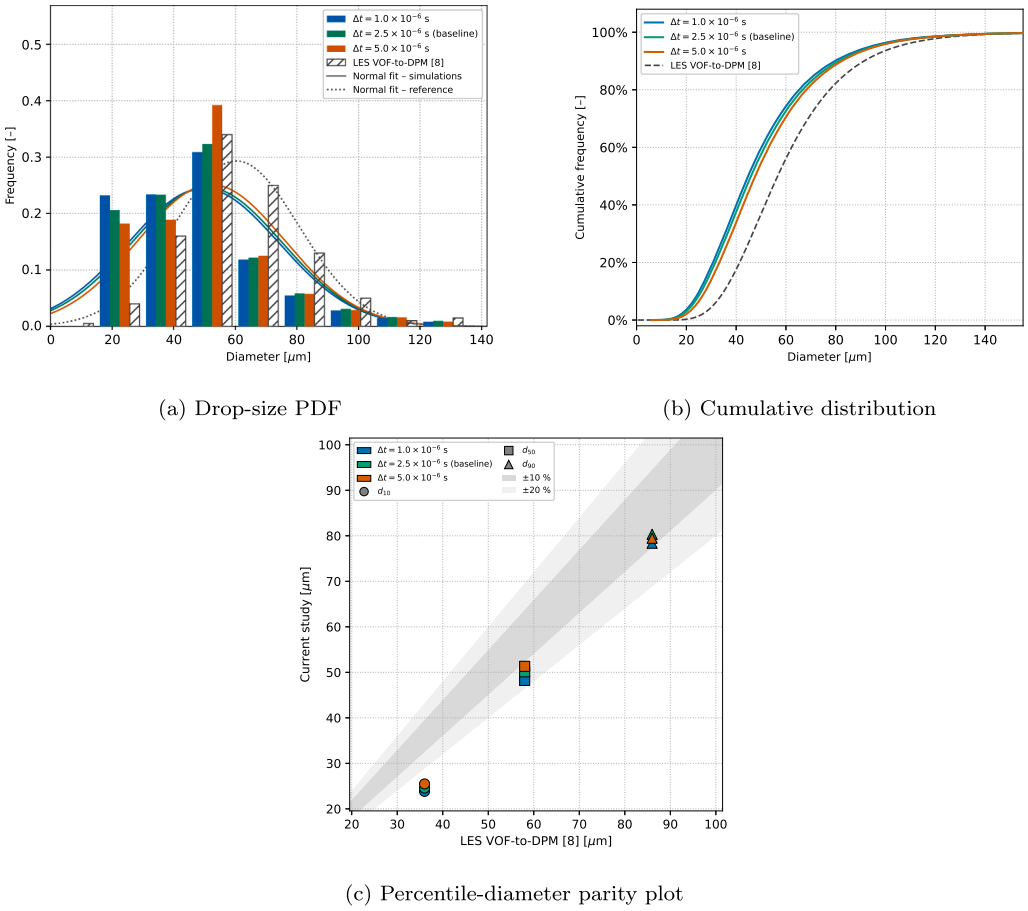
Computational domains and meshes for TC1 and TC2 are reported in Fig. 4. A sectional cutting plane through the domain is also included to clearly highlight the mesh refinement regions.

3.4. Breakup model constants

The constants required by the Madabhushi model are determined here on the basis of established literature values and empirical correlations, taking advantage of the operating conditions introduced in the previous section.

Wave model constants. The empirical constant B_0, which relates the child particle radius to the wavelength of the fastest-growing Kelvin-Helmholtz instability through Eq. (14), is set to 2.44. This value is adopted following the work of Lambert et al. [44], providing a more accurate estimation of the initial fragment sizes in the context of liquid core stripping compared to the original Reitz formulation. The breakup time constant B_1, governing the Wave stripping timescale through Eq. (15), is set to 1.73. This value corresponds to the standard established in the KIVA code [37] and is widely utilized in the literature for Wave-based and models operating in the primary stripping regime.

Column drag coefficient. The drag coefficient of the liquid column governs the momentum exchange between the intact jet and the crossflow gas during the primary breakup phase, directly influencing the predicted particle trajectory. In the native Madabhushi formulation, the



(a) Drop-size PDF

(b) Cumulative distribution

(c) Percentile-diameter parity plot

Fig. 3. Time-step convergence at $We_g = 8500$: (a) drop-size probability density function, (b) cumulative distribution, and (c) parity of the percentile diameters, for $\Delta t = 1.0$, 2.5 (baseline) and 5.0×10^{-6} s compared with the LES VOF-to-DPM reference.

unresolved liquid column is represented by spherical blobs and a constant drag coefficient is applied until the column-breakup time [18,33]. This representation cannot reproduce the continuous evolution of the projected area and wake of a bending and deforming liquid column. Deformation-dependent and unsteady variations of drag have been reported for both droplets and liquid columns [34–36]. Consequently, the fixed spherical-blob coefficient may under-represent the effective aerodynamic loading during portions of the pre-breakup history.

The present work does not attempt to derive a complete deformation-dependent column-drag law. Instead, a preliminary projected-area closure is introduced to assess the effect of an increased column-phase loading within the existing Lagrangian formulation. The drag force acting on the spherical numerical carrier is written as:

$$F_D = \frac{1}{2}\rho_g u_{rel}^2 C_{D,eff} A_p, \qquad A_p = \frac{\pi}{4} D^2, \tag{32}$$

and the effective coefficient is defined through the drag-area mapping:

$$C_{D,eff} A_p = C_{D,col} A^*_{col}, \tag{33}$$

where A^*_{col} denotes a representative projected area of the unresolved column element. For the first assessment, a projected width D and a representative projected length $L_r = D$ are assumed, giving

$$A^*_{col} = D L_r = D^2, \qquad C_{D,eff} = \frac{4}{\pi} C_{D,col}. \tag{34}$$

Using $C_{D,col} = 1.696$, consistently with the cylindrical-element trajectory analysis of Wu et al. [53], gives $C_{D,eff} \simeq 2.16$.

Eq. (34) maps only the drag-area product under an explicit representative-column assumption. It is not a strict force- or acceleration-equivalence derivation between a spherical parcel and a physical column segment, for which no unique correspondence in mass, length or instantaneous geometry exists. The proposed value is therefore treated as a preliminary closure and not as a universal or final coefficient. It is imposed only while a parcel represents the unresolved liquid column; after the column-breakup time, the native drag and breakup treatment of the resulting fragments is left unchanged.

The uncertainty associated with the projected-area assumption is assessed by perturbing $C_{D,eff}$ by ±30% while retaining all other physical and numerical settings. The resulting values are 1.51, 2.16 and 2.81; the lower value is close to the native Madabhushi coefficient. The assessment is performed at both TC2 Weber numbers and is based on the spatially resolved transverse diameter profiles, as discussed in Section 5.3.

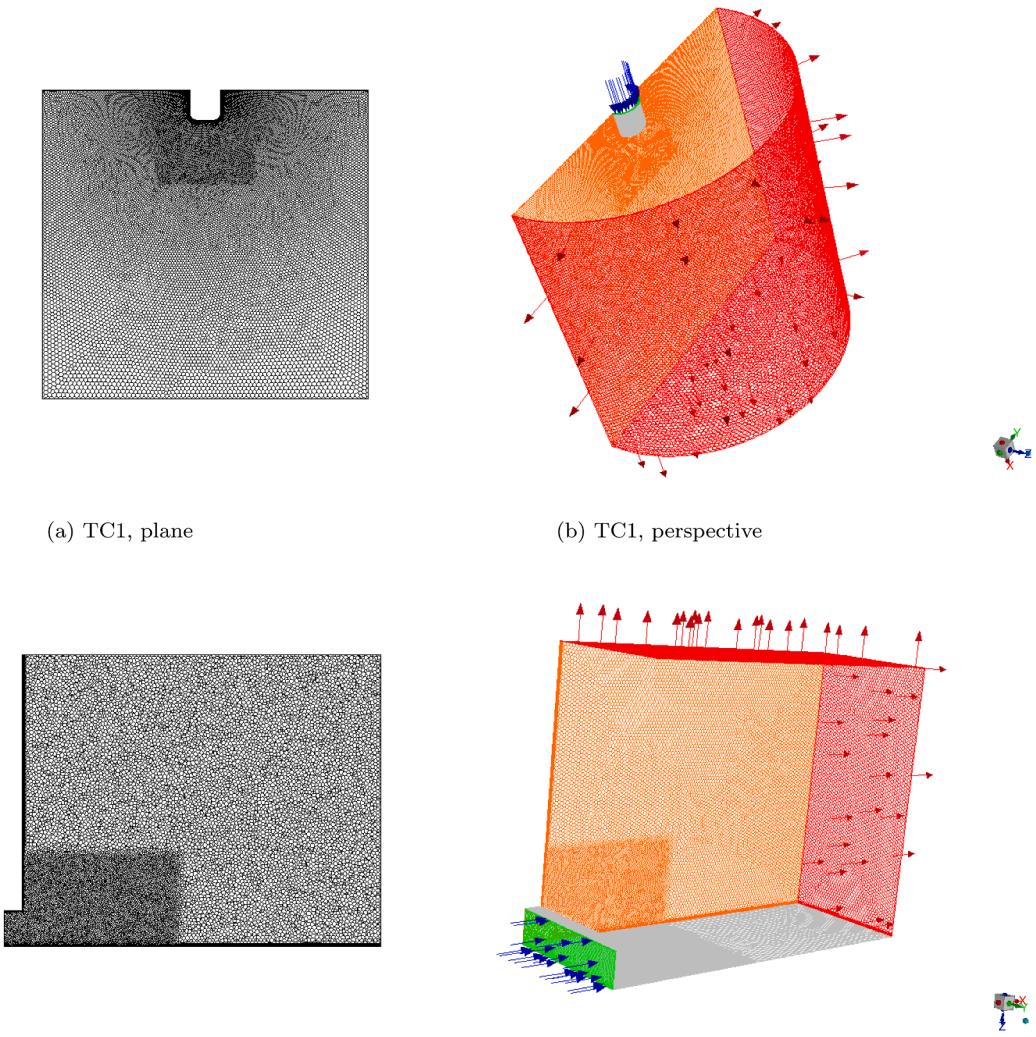
Column breakup time constant. The column breakup time t_{cb}, defined through the constant $C_0 = t_{cb}/t^*$ with reference timescale $t^* = (\rho_l/\rho_g)^{0.5} d/u_g$ [54], marks the transition in the Madabhushi model from Wave stripping to Pilch-Erdman secondary fragmentation. Rather than adopting a fixed value, C_0 is evaluated from empirical correlations matched to the operating conditions of each test case.

For TC2-W1 and TC2-W2, C_0 is obtained from the correlation of Lubarsky et al. [55]:

$$C_0 = 9.98 - 0.908 \ln(Re_j), \tag{35}$$

where $Re_j = \rho_l w_j d/\mu_l$ is the liquid jet Reynolds number. This correlation was found to produce consistent results for the TC2 operating conditions and is applied directly.

For TC1-P1 and TC1-P2, characterized by a very low momentum-flux ratio, the short column-breakup length limits the development of the internal jet turbulence that Eq. (35) is designed to capture. For these



(a) TC1, plane

(b) TC1, perspective

(c) TC2, plane

(d) TC2, perspective

Fig. 4. Computational domains with mesh for TC1 and TC2 test cases.

cases C_0 is therefore evaluated a priori from the correlation of Shaw et al. [56], which includes an explicit dependence on the momentum-flux ratio q:

$$C_0 = 0.886\, q^{-0.233}\, We_{\text{aero}}^{-0.218}, \tag{36}$$

where $We_{\text{aero}} = \rho_g w_j^2 d/\sigma$. The resulting C_0 values for each test case are reported in Table 6. In this way the column-breakup constant is not treated as a free parameter but is tied to operating-condition correlations, each associated with one of the two breakup regimes spanned by the test matrix (the low momentum-flux ratio regime of TC1 and the higher-q, turbulence-driven regime of TC2). Selecting the correlation a priori from the injection conditions reduces the calibration uncertainty with respect to the use of a single, case-independent value, which is the sense in which the constant set is regarded as consistent across the operating range.

Ligament factor. The ligament factor F_{lig}, introduced by Lambert et al. [44] as an extension of the original Madabhushi formulation [33], represents the diameter ratio between the ligaments produced at the column breakup point and the parent liquid column (see Eq. (28)). After column breakup at t_{cb}, parent parcels are partitioned into child droplets of diameter D_{lig}, which subsequently undergo Pilch-Erdman secondary fragmentation [32] based on their local droplet Weber number. The value of F_{lig} therefore directly controls the initial size of the spray entering the secondary breakup cascade.

Lambert et al. [44] adopted $F_{lig} = 0.4$ for operating conditions in the shear-stripping regime ($We_g > 350$ [32]). All test cases considered in the present work feature gas Weber numbers well within this regime, and the value $F_{lig} = 0.4$ is therefore adopted throughout without further calibration.

A summary of all model constants adopted in the present simulations is provided in Table 6.

3.5. Fluid properties

The thermophysical properties adopted for the three fluid species are summarised in Table 7. Air and nitrogen are modeled as ideal gases, with density computed through the ideal gas law. Water is treated as an incompressible liquid with constant properties evaluated at standard conditions, given the non-evaporating conditions.

3.6. Numerical schemes

The simulations were carried out by using ANSYS Fluent 2025R1, employing a pressure-based solver with the PISO (Pressure-Implicit with Splitting of Operators) algorithm for pressure–velocity coupling. The

Table 6
Final simulation matrix with Madabhushi model constants adopted in the present simulations.

	B_0	B_1	C_D	C_0	F_{lig}
TC1-P1	2.44	1.73	2.16	0.85	0.4
TC1-P2	2.44	1.73	2.16	0.78	0.4
TC2-W1	2.44	1.73	2.16	0.87	0.4
TC2-W2	2.44	1.73	2.16	0.46	0.4

Table 7
Fluid properties adopted in the simulations.

Property	Symbol	Air	Nitrogen	Water
Density	ρ [kg/m^3]	Ideal gas	Ideal gas	998.2
Specific heat	c_p [J/kg·K]	1006.43	1040.67	4182
Dynamic viscosity	μ [kg/m·s]	1.789×10^{-5}	1.663×10^{-5}	1.003×10^{-3}
Thermal conductivity	k [W/m·K]	0.0242	0.0242	0.600
Molar mass	M [g/mol]	28.966	28.014	18.015
Surface tension	σ [N/m]	–	–	0.073

Madabhushi column-breakup model and the Lambert ligament correction are invoked as native modules of this release, and no user-defined function is employed; the five-fragment count, the root-normal child-size distribution and the ligament weighting therefore correspond to the standard native implementation. Spatial discretization of all governing equations was performed using a second-order upwind scheme, while time advancement was handled through a second-order implicit formulation.

The integration of Eqs. (5) and (7), which constitute a set of coupled ordinary differential equations, was performed using a solver that dynamically switches between a low-order implicit Euler scheme and a high-order trapezoidal scheme. During runtime, the solver automatically selects the appropriate scheme: high-order schemes are applied when particles are far from hydrodynamic equilibrium, allowing accurate solutions with fewer step refinements, whereas low-order schemes are employed near equilibrium, where high-order schemes become inefficient due to limited stable step lengths [18]. After a series of preliminary tests, this configuration was selected as it provided the best compromise between stability and computational efficiency. Accuracy control with a tolerance of $\epsilon = 10^{-5}$ was additionally employed to automatically adjust the Lagrangian timestep during the integration of Eqs. (5) and (7), ensuring that each integration step satisfies the prescribed error threshold while minimizing unnecessary refinements.

A preliminary steady-state computation was conducted to initialize the flow field under undisturbed conditions. This initialization step was adopted to improve numerical stability prior to the transient calculation. Subsequently, a transient simulation was performed to model the injection of water into the crossflow.

4. Numerical data processing

Numerical data post-processing is essential in Lagrangian spray simulations to extract meaningful statistics and interpret the spatial, temporal, and case-dependent variability inherent to stochastic models. For all the test cases, the simulation is first advanced until the number of computational parcels present in the domain reaches an approximately stationary value, identified by the equilibrium of the rates of parcel injection, escape, coalescence, and breakup within the domain. Time-averaged droplet statistics are then collected over a subsequent sampling window, during which lagrangian quantities of interest are monitored to verify that a statistically stationary state has been reached.

4.1. TC1

Droplet statistics for TC1 are collected on a series of rectangular sampling planes oriented perpendicular to the crossflow direction and distributed at the measurement locations reported in the reference experimental study. Each plane has a size of 20 mm, matching the diameter of the laser measurement beam used in the experiments, so as to ensure a consistent spatial averaging between the numerical and experimental datasets. Parcel data crossing each plane during the sampling window are accumulated and post-processed to yield mass-flow-weighted D_{32}.

4.2. TC2

For TC2, droplet statistics are extracted on sampling planes following the same procedure described for TC1, at streamwise locations corresponding to those reported in the reference LES VOF-to-DPM data. At each downstream location x/d, parcels are binned in the wall-normal direction z using a uniform bin size of $\Delta z = 5$ mm, chosen to provide adequate spatial resolution across the domain height of 65 mm. The resulting profiles of D_{32}, D_{10} and droplet velocities are compared against the reference data at each downstream location. Moreover, the droplet size distribution at selected downstream locations is characterized through the probability density function (PDF) of droplet diameters and the corresponding cumulative frequency distribution, from which the characteristic diameters d_{10}, d_{50}, and d_{90} are extracted as the droplet sizes at the 10th, 50th, and 90th percentile of the cumulative number distribution, respectively.

5. Results and discussion

In this Section, results are presented and discussed.

5.1. TC1

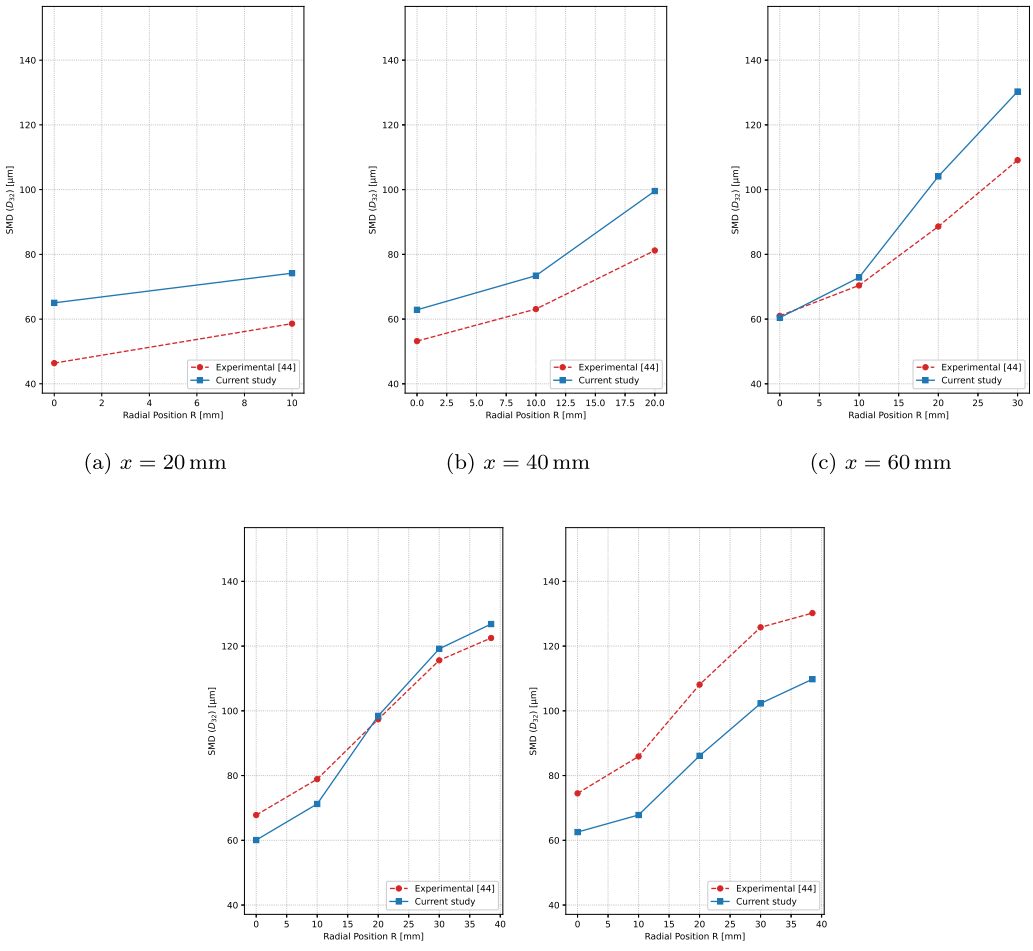
5.1.1. SMD at different downstream and radial locations

The predictive accuracy of the numerical model regarding the spray atomization characteristics is evaluated through both localized radial profiles and parity plots. The radial distributions of the droplet SMD at fixed downstream axial locations are reported in Figs. 5 and 6 for cases TC1-P1 and TC1-P2, respectively. Complementarily, Fig. 7 provides the global parity plots, categorized by radial position (R) and axial plane (x).

As observed in Figs. 5 and 6, the numerical model demonstrates a high capability in capturing the macroscopic spatial evolution of the spray. The calculated radial trends are in good qualitative agreement with the experimental data for both test cases across all investigated downstream locations. Specifically, the model correctly predicts a monotonic increase in D_{32} with respect to the radial coordinate (R). This consistent outward growth is physically driven by two main mechanisms reported by the experimental work's authors [50]:

- Aerodynamic Sorting: the vertical acceleration experienced by a droplet is inversely proportional to its diameter. Consequently, smaller droplets respond dynamically faster to the high-velocity gas core, acquiring high axial velocities and remaining confined near the spray centerline ($R < 15$ mm). Conversely, larger droplets possess higher inertia, allowing them to resist core entrainment and migrate toward the spray periphery.
- Gas Diffusion and Drag Decay: as the continuous phase expands radially, its velocity decays due to momentum diffusion, leading to a localized drop in aerodynamic drag. This reduction in shear stress allows larger droplets to persist at high radial coordinates without undergoing further secondary breakup.

Despite successfully reproducing the radial gradients, the model exhibits two opposite local deviations, as highlighted by the parity charts: it tends to overpredict D_{32} in the near-field and near-axis region (x = 20-60 mm) and to underpredict it in the far field (x = 80-100 mm). This behavior is consistent with the way blob injection and the single-mechanism secondary breakup reproduce the atomization along the trajectory. Because blob injection replaces the primary breakup with a progressive stripping of the liquid column, the fine-droplet population is



(a) $x = 20\,\text{mm}$ (b) $x = 40\,\text{mm}$ (c) $x = 60\,\text{mm}$

(d) $x = 80\,\text{mm}$ (e) $x = 100\,\text{mm}$

Fig. 5. SMD results at various downstream (x) and radial (R) locations for TC1-P1 test case.

generated gradually downstream: near the injector the modeled spray is therefore coarser than the measurements, which already contain the fine droplets produced by primary atomization, and the D_{32} is biased high in the near-field, near-axis region. Farther downstream, the cumulative Wave/Pilch-Erdman stripping progressively over-fragments the surviving droplets, the same tendency to overproduce fine droplets observed at the lower Weber number for the TC2 cases, so that D_{32} falls below the measurements in the far field. A comparable difficulty of the purely Lagrangian approach in reproducing, on its own, the column breakup and shedding of jets in crossflow, together with an underprediction of D_{32} where the local droplet velocity is overpredicted, has been reported in the literature [42]. With a parcel population of the order of 10^6, about an order of magnitude above the values commonly adopted in Lagrangian spray studies, statistical under-resolution of the dispersed phase is not expected to be the controlling factor; a residual near-field uncertainty is instead associated with the locally dense character of the near-orifice region, where the dilute assumptions underlying the discrete-phase and collision models are stressed (see Section 2).

Overall, 29% of the data points lie within ±10% and 68% within ±20% of the experimental values (38 points).

5.2. TC2

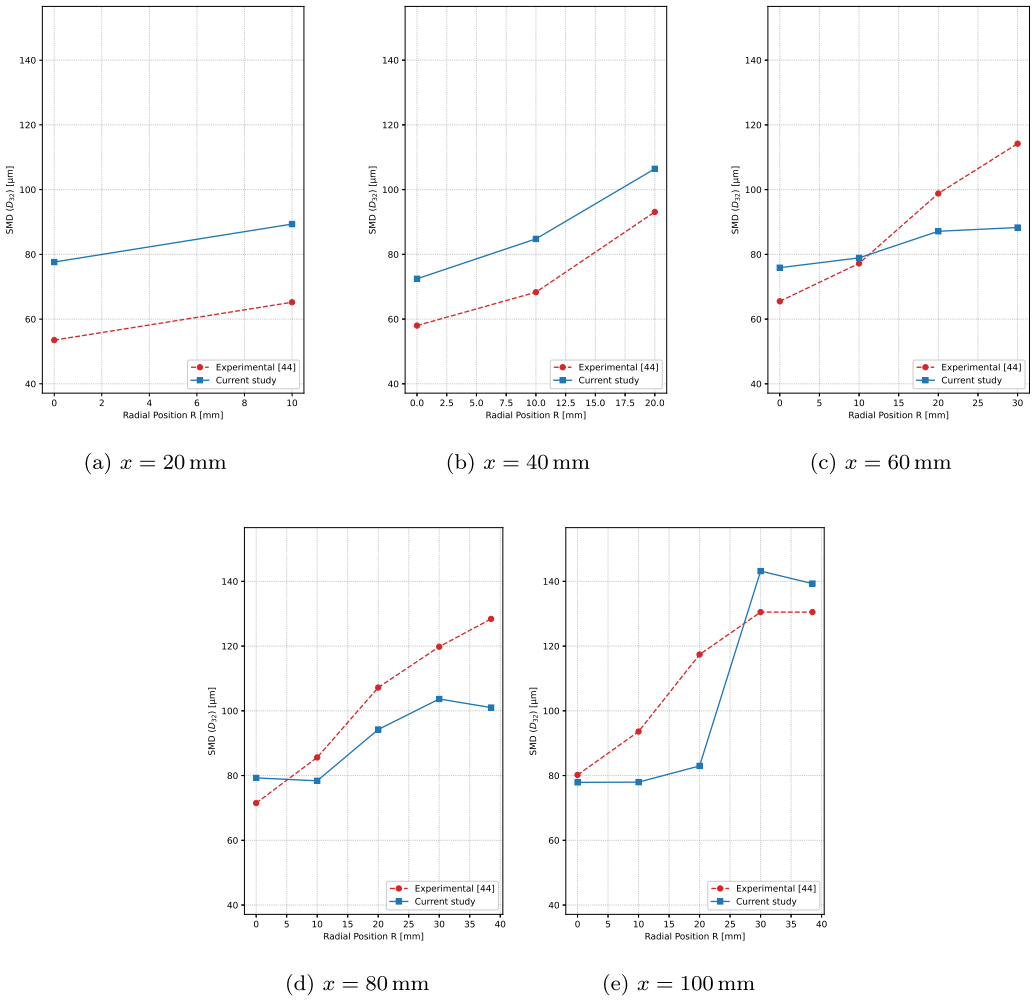
5.2.1. Droplet diameter profiles

Figs. 8 and 9 report the transverse profiles of the mean diameter D_{10} and the Sauter mean diameter D_{32} along the z-coordinate at $x = 60\,\text{mm}$ from the injector orifice for TC2-W1 and W2 test cases. Both descriptors exhibit a consistent set of trends across the throttling range: diameters decrease monotonically with increasing We_g, confirming the progressive intensification of aerodynamic fragmentation, and their spatial profiles grow along the z-axis as larger droplets produced by residual ligament breakup accumulate in the outer region of the spray.

At $\text{We}_g = 3500$, D_{32} rises from approximately 55 μm at $z = 2.5\,\text{mm}$ to 125 μm at $z = 57.5\,\text{mm}$, and both D_{10} and SMD reproduce the gradual monotonic growth consistent with the numerical data. At $\text{We}_g = 8500$, D_{32} increases more slowly from 52 μm to 110 μm over the same axial range. D_{10} follows a qualitatively identical behavior at both conditions, with lower absolute values, and the present results remain within the scatter of the reference at all radial stations. Relative to the LES reference, the present transverse profiles rise more steeply and monotonically along z, whereas the reference profiles are flatter, so that the two sets cross at around $z = 30\,\text{mm}$, with the present results lying below the reference near the axis and above it in the far field.

5.2.2. Particle velocity

Fig. 10 shows the radial profiles of mean droplet axial velocity U as a function of z for the two Weber number conditions. The present results correctly capture the dominant physical trends: U decreases monotonically from the injection plane outward at all We_g, and near-field droplet velocities scale approximately linearly with the gas Weber number, reaching $\sim 140\,\text{m/s}$, $\sim 90\,\text{m/s}$ near the jet axis for $\text{We}_g = 8500$ and 3500, respectively. The shape of the deceleration profile, which is a steep drop in the near field followed by a gradual leveling-off beyond the gas-film coverage height, is well reproduced at all conditions, confirm-



(a) $x = 20\,\text{mm}$ (b) $x = 40\,\text{mm}$ (c) $x = 60\,\text{mm}$

(d) $x = 80\,\text{mm}$ (e) $x = 100\,\text{mm}$

Fig. 6. SMD results at various downstream (x) and radial (R) locations for TC1-P2 test case.

ing that the Lagrangian drag model captures the essential aerodynamic exchange between the dispersed and carrier phases.

Quantitatively, the present predictions exceed the LES VOF-to-DPM reference in the near field, with differences of approximately 50-60% at the first sampling station for $\text{We}_g = 3500$ and 8500, in line with an underprediction of the diameters in this zone. In the far field ($z > 30\,\text{mm}$), the two profiles converge toward comparable values for all Weber numbers. This behavior is known in Euler-Lagrange simulations, both RANS [33] and scale-resolved simulations [44], and the maximum errors are in line with these other studies. Since the near-field droplet momentum contributes to the impingement conditions and to the near-wall droplet flux relevant to the wall heat load, this near-field overprediction should be accounted for whenever the model is used for impingement- or heat-flux-critical estimates in the first few orifice diameters; the downstream and global spray statistics, which are the primary target of the present framework, are instead reproduced reliably.

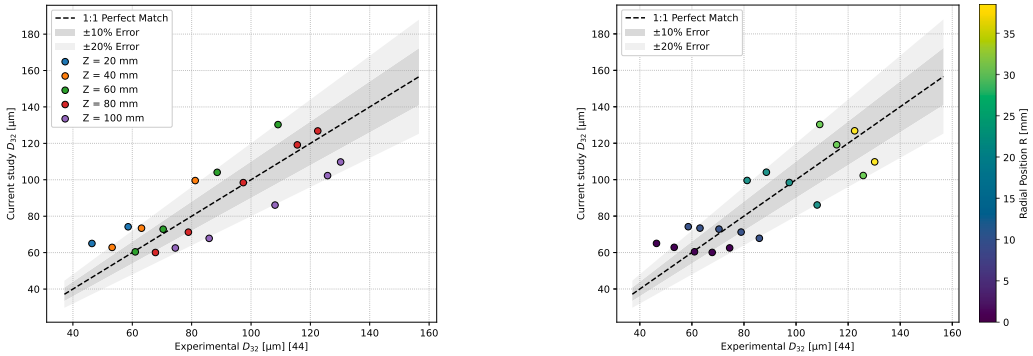
5.2.3. Statistical analysis

The probability density functions (PDFs) of droplet diameter at $x = 60\,\text{mm}$ downstream of the injection point are shown in Fig. 11 for TC2-W1 and W2, together with Gaussian fits and the LES VOF-to-DPM reference histograms. In all cases the present results reproduce the correct unimodal character of the distribution and the systematic shift of the mode toward smaller diameters with increasing We_g. At $\text{We}_g = 3500$, the mode shifts to $\sim 50\,\mu\text{m}$ in the present results against $\sim 75\,\mu\text{m}$ in the LES, with comparable peak amplitudes (0.39 vs. 0.41). At $\text{We}_g = 8500$, the two PDFs achieve the closest overall agreement: the mode locations differ by less than one bin width and the peak amplitudes agree within 6% (0.32 vs. 0.34), with the Gaussian fits converging rapidly beyond $d \approx 80\,\mu\text{m}$. The systematic trend of improving distributional agreement with We_g is consistent with the progressive simplification of the breakup physics toward a single mechanism that the Lagrangian framework captures well.

The cumulative frequency distributions (CDFs) in Fig. 12 confirm the above picture and allow a direct quantification of the percentile accuracy at the measurement plane. At $\text{We}_g = 3500$, the present CDF leads the reference, reaching $\sim 90\%$ at $d \approx 75\,\mu\text{m}$ against $\sim 63\%$ in the LES, but both approach unity at the same maximum diameter of $\sim 200\,\mu\text{m}$, demonstrating that the primary injection length scale provides the correct constraint on the coarse tail of the distribution regardless of the distributional shift at intermediate sizes. At $\text{We}_g = 8500$, the offset between the two CDFs is smaller and both reach unity at $d \approx 140\,\mu\text{m}$.

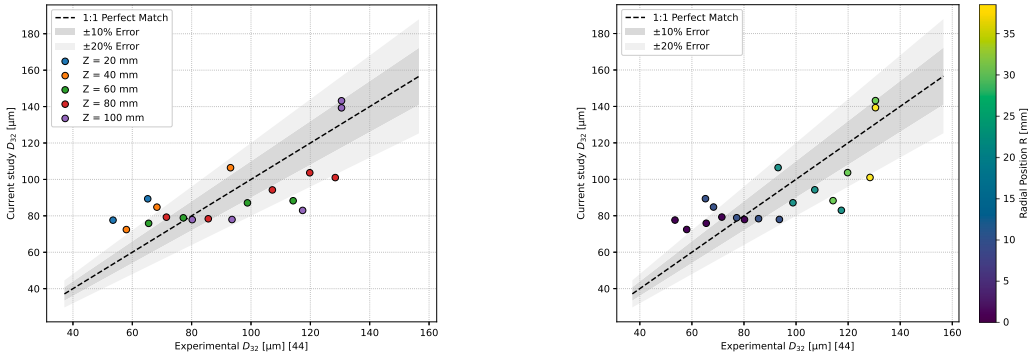
Across all conditions, the good reproduction of the maximum droplet diameter and the correct monotonic dependence of the CDF on We_g confirm that the Lagrangian URANS framework provides a physically consistent and computationally tractable description of the spray statistics in gas-liquid pintle injectors over a wide range of throttling levels.

The parity plots in Fig. 13 compare the 10th, 50th, and 90th percentile diameters (d_{10}, d_{50}, d_{90}), extracted at $x = 60\,\text{mm}$ downstream of the injection point, against the LES VOF-to-DPM reference, with $\pm 10\%$ and $\pm 20\%$ tolerance bands. The overall behavior is consistent across all the Weber number conditions, with the majority of the data points falling within or near the $\pm 20\%$ interval. At $\text{We}_g = 3500$, the d_{90} agrees within $\pm 10\%$ (98 vs. 109 μm), confirming that the large-droplet tail, which sets the spray penetration depth and influences the local liquid volume fraction, is correctly bounded by the primary injection model. The d_{50} prediction ($\sim 56\,\mu\text{m}$) lies approximately 22% below the reference



(a) TC1-P1, axial

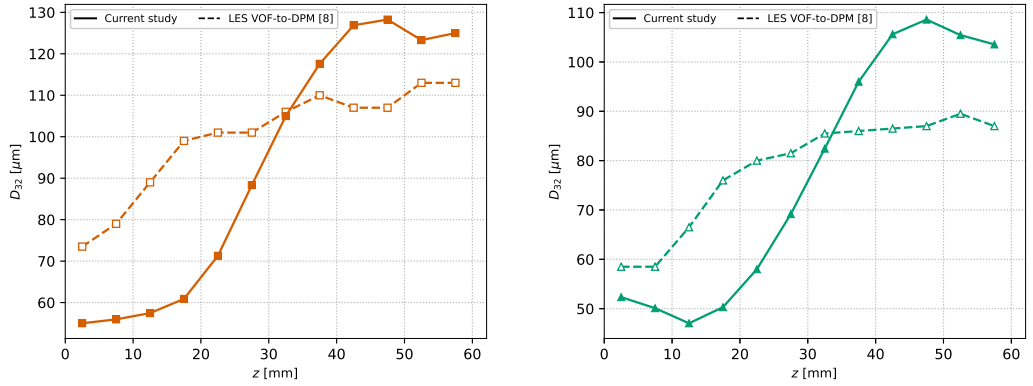
(b) TC1-P1, radial



(c) TC1-P2, axial

(d) TC1-P2, radial

Fig. 7. Parity plot of SMD results for TC1 test cases.



(a) $\mathrm{We}_g = 3500$

(b) $\mathrm{We}_g = 8500$

Fig. 8. D_{32} at $x = 60$ mm downstream location for TC2 test cases.

(72 μm), and the d_{10} is correspondingly shifted toward smaller values, reflecting an overproduction of fine droplets through shear stripping relative to the VOF-resolved intermediate-size population generated by ligaments. This shift is consistent with the known sensitivity of the intermediate percentiles to the multimode breakup.

At $\mathrm{We}_g = 8500$ the agreement improves further: d_{50} and d_{90} fall within the ±20% and ±10% bands respectively (50 vs. 58 μm and 80 vs. 86 μm), and the residual underprediction of d_{10} (25 vs. 36 μm) is physically attributable to the fine-droplet population.

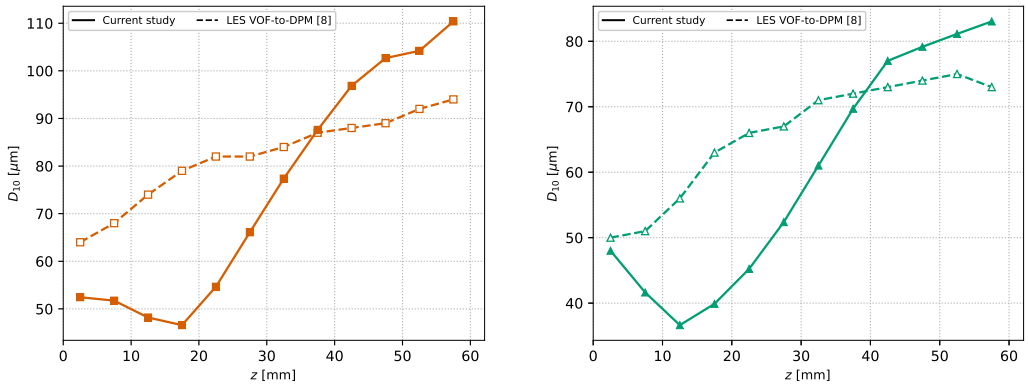
5.3. Sensitivity to the effective column drag coefficient

The sensitivity of the spatially resolved spray predictions to the effective column drag coefficient was assessed at both TC2 operating conditions. Three values were considered: $C_{\mathrm{D,eff}} = 1.51$, 2.16, and 2.81, corresponding to a ±30% variation about the nominal value. The lower value is close to the constant coefficient employed in the native Madabhushi column-phase formulation, whereas the central value corresponds to the preliminary projected-area correction introduced in Section 3.4. All other physical and numerical parameters were kept unchanged.

The comparison was performed using the transverse D_{10} and D_{32} profiles at the TC2 sampling section. The agreement with the LES VOF-to-DPM reference was quantified through the normalized root-mean-square error:

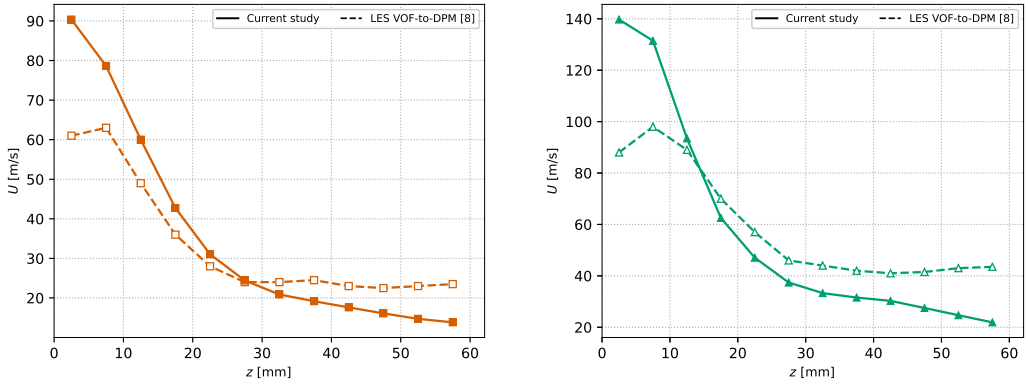
$$\mathrm{NRMSE}_\phi = 100 \frac{\left[N_z^{-1} \sum_{j=1}^{N_z} \left(\phi_{\mathrm{sim},j} - \phi_{\mathrm{ref},j} \right)^2 \right]^{1/2}}{N_z^{-1} \sum_{j=1}^{N_z} \left| \phi_{\mathrm{ref},j} \right|} \tag{37}$$

where ϕ denotes either D_{10} or D_{32} and N_z is the number of transverse sampling positions.



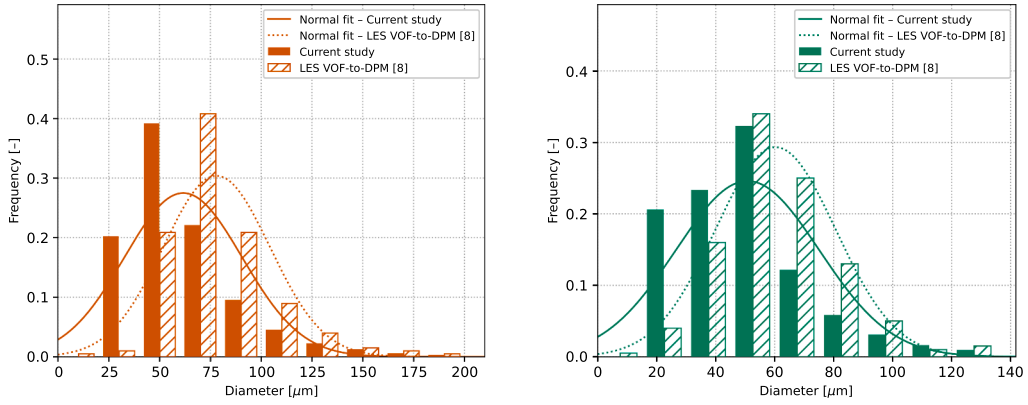
(a) $\mathrm{We}_g = 3500$ (b) $\mathrm{We}_g = 8500$

Fig. 9. D_{10} at $x = 60$ mm downstream location for TC2 test cases.



(a) $\mathrm{We}_g = 3500$ (b) $\mathrm{We}_g = 8500$

Fig. 10. Particles velocity magnitude downstream location for TC2 test cases.

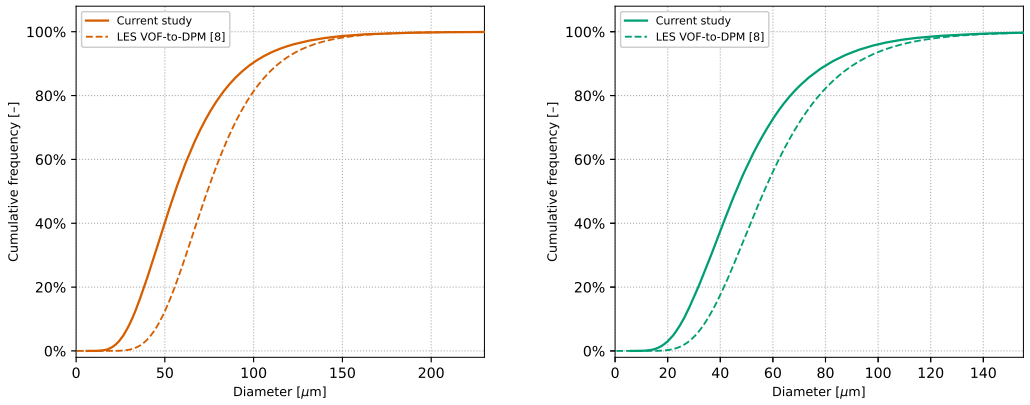


(a) $\mathrm{We}_g = 3500$ (b) $\mathrm{We}_g = 8500$

Fig. 11. Probability density function at $x = 60$ mm downstream location for TC2 test cases.

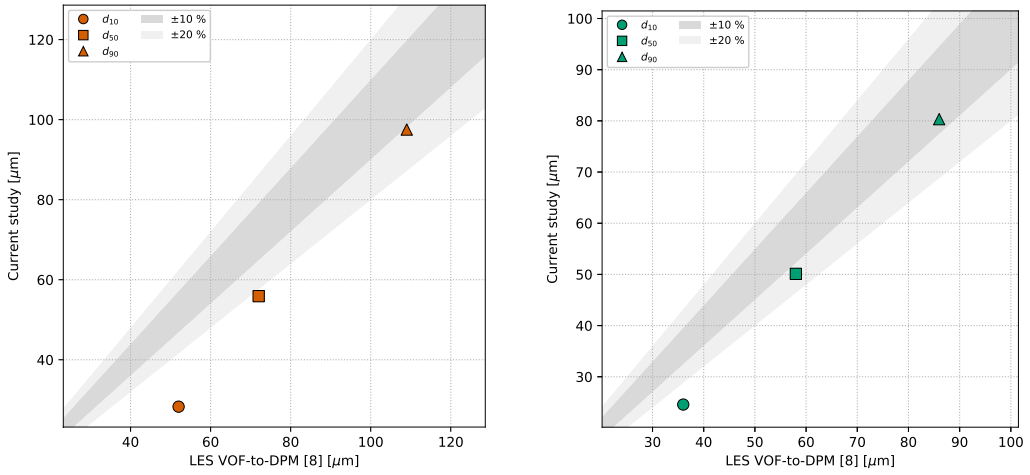
As reported in Table 8, the nominal coefficient provides the lowest D_{32}-profile error at both Weber numbers. At $\mathrm{We}_g = 3500$, the D_{10} errors obtained with the lower and nominal coefficients are nearly identical, while the higher coefficient produces a moderate deterioration. At $\mathrm{We}_g = 8500$, the nominal value also gives the lowest D_{10} error. The central coefficient therefore provides the most consistent agreement across the two profile quantities and operating conditions considered.

The response is not monotonic with the prescribed coefficient. In particular, increasing $C_{\mathrm{D,eff}}$ beyond the nominal value does not lead to a systematic improvement of either profile. This behavior is consistent with the role of the coefficient within the Madabhushi breakup sequence. The modified drag acts only while the parcel represents the unresolved liquid column, during which the column trajectory, gas-liquid relative motion, and Wave stripping history are established. The residual parent liquid then undergoes Pilch-Erdman fragmentation, followed by the transport and interaction of the resulting parcels [18,33]. Consequently, changes in column-phase drag are transmitted to the downstream diameter field through several coupled mechanisms and do not define a direct or universally monotonic variation of the local droplet diameter.



(a) $\mathrm{We}_g = 3500$ (b) $\mathrm{We}_g = 8500$

Fig. 12. Cumulative function at $x = 60$ mm downstream location for TC2 test cases.



(a) $\mathrm{We}_g = 3500$ (b) $\mathrm{We}_g = 8500$

Fig. 13. Parity plots of d_{10}, d_{50} and d_{90} at $x = 60$ mm for TC2 test cases.

Table 8
Sensitivity of the transverse diameter profiles to the effective column drag coefficient. The reported values are the NRMSE with respect to the TC2 LES VOF-to-DPM reference and are expressed in percent.

We_g	Quantity	$C_{\mathrm{D,eff}} = 1.51$	$C_{\mathrm{D,eff}} = 2.16$	$C_{\mathrm{D,eff}} = 2.81$
3500	D_{10}	21.47	21.84	23.04
	D_{32}	23.40	21.47	24.60
8500	D_{10}	24.29	19.25	22.70
	D_{32}	25.09	20.96	23.70

Previous Euler-Lagrange spray calculations have similarly shown that changes in aerodynamic drag may alter downstream diameter predictions through their coupling with breakup and coalescence, rather than through a direct drag-size relationship [37]. The present results are consistent with this interpretation: the proposed correction improves the spatial distribution of D_{32} at both Weber numbers and provides either comparable or improved D_{10} agreement, whereas a further increase of the coefficient gives no systematic advantage.

Overall, among the three values investigated, $C_{\mathrm{D,eff}} = 2.16$ provides the most consistent spatially resolved agreement with the TC2 reference data. The sensitivity analysis therefore supports its use as a preliminary effective column-phase closure for the present operating conditions. The limited and non-monotonic response also indicates that the proposed value should not be interpreted as a uniquely optimal or universally applicable drag coefficient. A more general closure would require an explicit dependence on the evolving column geometry and independent validation against column-trajectory and breakup-location measurements.

6. Conclusions

A Euler-Lagrange URANS methodology has been developed and assessed for the simulation of cold-flow atomization in discrete-orifice gas-liquid pintle injectors. The approach combines blob injection with the Madabhushi secondary breakup model, with the Lambert ligament correction, and requires no interface-resolving treatment of the primary atomization region. The calibration uncertainty of the breakup-model coefficients has been reduced by tying them to operating-condition correlations, so that in particular the column-breakup constant is determined a priori from the injection conditions rather than from case-independent free values. Validation against both experimental measurements and high-fidelity LES VOF-to-DPM reference solutions yields the following principal findings.

- The model reproduces the macroscopic radial evolution of D_{32} in good agreement with experimental data across all investigated downstream locations. The monotonic outward diameter growth,

governed by aerodynamic sorting between the high-velocity gas core and the outer low-shear region, is correctly predicted in both magnitude and spatial structure, with the majority of data points falling within the ±20% tolerance band. Locally, the model tends to overpredict D_{32} in the near-field and near-axis region and to underpredict it in the far field.

- A systematic underestimation of D_{32} is observed near the spray axis in the early development region, where adjacent orifice spray fields overlap at high parcel number densities. These local deviations are attributed to the blob-injection and single-mechanism secondary-breakup modeling rather than to a statistical limitation of the Lagrangian framework: the fine-droplet population is generated gradually along the trajectory, biasing D_{32} high near the injector and low in the far field.
- Against the LES VOF-to-DPM reference, good agreement is achieved at $We_g = 3500$ and 8500 in the distributional and integral statistics (D_{10}, D_{32}, droplet velocity profiles, probability density functions, cumulative distributions, and percentile diameters), with local pointwise deviations along the transverse profiles. The progressive improvement in accuracy with gas Weber number reflects the progressive simplification of the breakup physics toward a single dominant mechanism, which is, the Kelvin-Helmholtz shear stripping, that the Lagrangian submodel can represent faithfully.
- The profile-based column-drag sensitivity gives a metric- and condition-dependent response. Among the three values investigated, the nominal coefficient gives the lowest transverse D_{32}-profile NRMSE at both Weber numbers; the D_{10} agreement is essentially unchanged at $We_g = 3500$ and improves at $We_g = 8500$, while a further increase gives no systematic benefit. The value $C_{D,eff} = 2.16$ is therefore retained as a preliminary bounded column-phase closure rather than as an optimal or universal drag correlation.
- The correct reproduction of maximum droplet diameter, the monotonic dependence of the size distribution on We_g, and the convergence of far-field velocity profiles across all conditions confirm that the proposed framework provides a physically consistent and computationally tractable description of spray statistics in gas-liquid pintle injectors over a wide range of throttling levels.

Overall, the results establish that a fully Lagrangian URANS formulation augmented by physical correlations, with breakup constants determined a priori from operating-condition correlations, can serve as a reliable and efficient tool for parametric atomization studies in throttleable liquid propellant injectors, where the cost of scale-resolving or interface-resolving simulations remains prohibitive for design-oriented investigations given the strict grid and, consequently, time step requirements. A deformation-dependent column-drag closure based on the evolving projected area or aspect ratio, and independently validated against column-trajectory and breakup-location measurements, remains a subject for future work.

CRediT authorship contribution statement

Leonardo Stumpo: Writing – original draft, Visualization, Validation, Methodology, Investigation, Formal analysis, Data curation, Conceptualization; **Andrea Ferrero:** Writing – review & editing, Validation, Supervision, Software, Resources, Project administration, Methodology, Funding acquisition, Formal analysis, Conceptualization; **Filippo Masseni:** Writing – review & editing, Validation, Supervision; **Dario Pastrone:** Writing – review & editing, Validation, Supervision.

Declaration of competing interest

The authors declare that they have no known competing financial interests or personal relationships that could have appeared to influence the work reported in this paper.

Acknowledgements

This work was supported by the Italian Ministry of University and Research (MIUR) under the PRIN 2022 research project *NextGenSProDesT - Next Generation Space Propulsion Design Techniques*. The authors gratefully acknowledge this support.

Data availability

Data will be made available on request.

References

[1] G. Dressler, J. Bauer, TRW pintle engine heritage and performance characteristics, 2012. https://doi.org/10.2514/6.2000-3871
[2] G. Dressler, Summary of deep throttling rocket engines with emphasis on apollo LMDE, 2012. https://doi.org/10.2514/6.2006-5220
[3] N. Ashgriz, Handbook of Atomization and Sprays: Theory and Applications, SpringerLink : Bücher, Springer US, 2011. https://books.google.it/books?id=ARKo1wxcdgQC.
[4] S. Lee, J. Koo, Y. Yoon, Effects of skip distance on the spray characteristics of a pintle injector, Acta Astronaut. 178 (2021) 471–480. https://doi.org/10.1016/j.actaastro.2020.09.043
[5] L. Lucchese, J. Liberatori, D. Cavalieri, D. Simone, D. Liuzzi, M. Valorani, P.P. Ciottoli, Sensitivity analysis of a continuous-slit pintle injector to the chemical kinetics modeling. https://doi.org/10.2514/6.2025-1548
[6] Z. Li, Y. Zhou, P. Cheng, X. Bai, Q. Li, Flow and spray characteristics of a gas–liquid pintle injector under backpressure environment, Phys. Fluids 36 (4) (2024) 043314. https://doi.org/10.1063/5.0201668
[7] P. Cheng, Q. Li, H. Chen, Flow characteristics of a pintle injector element, Acta Astronaut. 154 (2019) 61–66. https://doi.org/10.1016/j.actaastro.2018.10.020
[8] M. Zhang, S. Zhou, L. Song, X. Zhang, J.-Y. Lyu, F. Dong, Atomization dynamics of gas-liquid orifice type pintle injectors at different throttling levels, Energy 335 (2025) 138192. https://doi.org/10.1016/j.energy.2025.138192
[9] Y. Jin, X. Xu, Q. Yang, S. Zhu, Numerical investigation of flame appearance and heat flux and in a deep-throttling variable thrust rocket engine, Aerosp. Sci. Technol. 88 (2019) 457–467. https://doi.org/10.1016/j.ast.2019.03.042
[10] J. Liberatori, R.M. Galassi, D. Liuzzi, A. Filosa, M. Valorani, P.P. Ciottoli, Injection of LOX spray in Methane cross-flow RANS modeling uncertainty quantification. https://doi.org/10.2514/6.2021-3570
[11] L. Lucchese, J. Liberatori, D. Cavalieri, D. Simone, D. Liuzzi, M. Valorani, P.P. Ciottoli, Impact of chemical modeling on the numerical analysis of a LOx/GCH4 rocket engine pintle injector, Acta Astronaut. 218 (2024) 240–250. https://doi.org/10.1016/j.actaastro.2024.02.038
[12] L. Lucchese, J. Liberatori, D. Cavalieri, D. Simone, D. Liuzzi, M. Valorani, P.P. Ciottoli, Radial mass flow rate partition on LOx/GCH4 pintle injector configurations, J. Propuls. Power 41 (2) (2025). 238–251. https://doi.org/10.2514/1.B39700
[13] F. Zhao, H. Zhang, H. Zhang, B. Bai, L. Zhao, Review of atomization and mixing characteristics of pintle injectors, Acta Astronaut. 200 (2022) 400–419. https://doi.org/10.1016/j.actaastro.2022.08.042
[14] A.H. Lefebvre, V.G. McDonell, Atomization and Sprays, CRC Press, 2017. https://books.google.it/books?id=80OEDgAAQBAJ.
[15] R.D. Reitz, F.V. Bracco, Mechanism of atomization of a liquid jet, Phys. Fluids 25 (10) (1982) 1730–1742. https://doi.org/10.1063/1.863650
[16] C.W. Hirt, B.D. Nichols, Volume of fluid (VOF) method for the dynamics of free boundaries, J. Comput. Phys. 39 (1) (1981) 201–225. https://doi.org/10.1016/0021-9991(81)90145-5
[17] S. Chadha, R. Jefferson-Loveday, T. Hussain, A high-fidelity simulation of the primary breakup within suspension high velocity oxy fuel thermal spray using a coupled volume of fluid and discrete phase model, Int. J. Multiph. Flow 133 (2020) 103445. https://doi.org/10.1016/j.ijmultiphaseflow.2020.103445
[18] ANSYS Inc., ANSYS Fluent Theory Guide, ANSYS Inc., 2025. Release 2025R1.
[19] H.G. Weller, G. Tabor, H. Jasak, C. Fureby, A tensorial approach to computational continuum mechanics using object-oriented techniques, Comput. Phys. 12 (6) (1998) 620–631.
[20] C.T. Crowe, D.E. Stock, M.P. Sharma, The particle-source-in cell /PSI-CELL/ model for gas-droplet flows, ASME J. Fluids Eng. 99 (1977) 325–332.
[21] P. Shi, G. Zhu, J. Cheng, J. Li, X. Hou, Simulation on atomization process of gas–liquid pintle injector in LRE under periodic conditions based on the VOF to DPM method, Aerosp. Sci. Technol. 136 (2023) 108222. https://doi.org/10.1016/j.ast.2023.108222
[22] B. Bhatia, T. Johny, A. De, Understanding the liquid jet break-up in various regimes at elevated pressure using a compressible VOF-LPT coupled framework, Int. J. Multiph. Flow 159 (2023) 104303. https://doi.org/10.1016/j.ijmultiphaseflow.2022.104303
[23] M. Zhang, X. Lei, F. Dong, S. Zhou, C. Wu, X. Lv, H. Liu, Atomization dynamics of gas-liquid orifice type pintle injector under different local momentum ratios, Aerosp. Sci. Technol. 168 (2026) 111179. https://doi.org/10.1016/j.ast.2025.111179
[24] R. Reitz, Modeling atomization processes in high-pressure vaporizing sprays, At. Spray Technol. 3 (1987) 309–337.
[25] J. Beale, R. Reitz, Modeling spray atomization with the Kelvin-Helmholtz/Rayleigh-Taylor hybrid model, At. Sprays 9 (1999) 623–650. https://doi.org/10.1615/AtomizSpr.v9.i6.40

[26] G.I. Taylor, The shape and acceleration of a drop in a high speed air stream, The Scientific Papers of G. I. Taylor (1963).
[27] M.A. Patterson, S.-C. Kong, G.J. Hampson, R.D. Reitz, Modeling the Effects of Fuel Injection Characteristics on Diesel Engine Soot and NOx Emissions, Tech. rep., SAE Technical Paper, 1994.
[28] C.J. Rutland, N. Ayoub, Z. Han, G. Hampson, S.-C. Kong, D. Mather, M. Musculus, M. Patterson, L. Ricart, P. Stephenson, et al., Progress Towards Diesel Combustion Modeling, Tech. rep., SAE Technical Paper, 1995.
[29] P. Yi, Y. Fu, T. Li, Effects of droplet evaporation on calibration of Kh-Rt break-up model for high-pressure evaporating diesel sprays, At. Sprays 32 (3) (2022) 1–23. https://doi.org/10.1615/AtomizSpr.2021038119
[30] R. He, P. Yi, T. Li, X. Zhou, Y. Gu, Evaluations of the Kh-Rt breakup and dynamic structure sgs models for evaporating sprays under diesel engine-like conditions, At. Sprays 30 (3) (2020) 189–212. https://doi.org/10.1615/AtomizSpr.2020033585
[31] R.D. Reitz, R. Diwakar, Structure of High-Pressure Fuel Sprays, Tech. rep., SAE Technical Paper, 1987.
[32] M. Pilch, C.A. Erdman, Use of breakup time data and velocity history data to predict the maximum size of stable fragments for acceleration-induced breakup of a liquid drop, Int. J. Multiph. Flow 13 (6) (1987) 741–757.
[33] R.K. Madabhushi, A model for numerical simulation of breakup of a liquid jet in crossflow, At. Sprays 13 (4) (2003) 413–424. https://doi.org/10.1615/AtomizSpr.v13.i4.50
[34] C. Shao, K. Luo, J. Fan, Detailed numerical simulation of unsteady drag coefficient of deformable droplet, Chem. Eng. J. 308 (2017) 619–631. https://doi.org/10.1016/j.cej.2016.09.062
[35] Y. Lin, J. Palmore, John, Effect of droplet deformation and internal circulation on drag coefficient, Phys. Rev. Fluids 7 (12) (2022) 123602. https://doi.org/10.1103/PhysRevFluids.7.123602
[36] T. Kamiya, M. Asahara, T. Miyasaka, Effect of a wake on drag and deformation of liquid column at high weber numbers, J. Fluid Sci. Technol. 15 (1) (2020) JFST0006. https://doi.org/10.1299/jfst.2020jfst0006
[37] A. Liu, D. Mather, R. Reitz, Modeling the effects of drop drag and breakup on fuel sprays (1993) 17. https://doi.org/10.4271/930072
[38] R. Ni, Deformation and breakup of bubbles and drops in turbulence, Annu. Rev. Fluid Mech. 56 (Volume 56, 2024) (2024) 319–347. https://doi.org/10.1146/annurev-fluid-121021-034541
[39] S.B. Pope, Turbulent Flows, Vol. 12, 2001. https://doi.org/10.1088/0957-0233/12/11/705
[40] F. Menter, J. Schutze, K. Kurbatskii, R. Lechner, M. Gritskevich, A. Garbaruk, Scale-Resolving Simulation Techniques in Industrial CFD. https://doi.org/10.2514/6.2011-3474
[41] J.J. Nijdam, B. Guo, D.F. Fletcher, T.A.G. Langrish, Lagrangian and Eulerian models for simulating turbulent dispersion and coalescence of droplets within a spray, Appl. Math. Model. 30 (11) (2006) 1196–1211. Selected papers from the Third International Conference on CFD in the Minerals and Process Industries. https://doi.org/10.1016/j.apm.2006.02.001
[42] M. Zghal, P. Gauthier, X. Sun, C. Wijesinghe, V. Sethi, Validation and assessment of a hybrid VOF-Lagrangian numerical methodology for turbulent liquid fuel jets in high-speed crossflow, J. Eng. Gas Turbines Power 146 (8) (2024). 081007. https://asmedigitalcollection.asme.org/gasturbinespower/article-pdf/146/8/081007/7236640/gtp_146_08_081007.pdf. https://doi.org/10.1115/1.4064218
[43] S.C.R. Dennis, S.N. Singh, D.B. Ingham, The steady flow due to a rotating sphere at low and moderate Reynolds numbers, J. Fluid Mech. 101 (2) (1980) 257–279. https://doi.org/10.1017/S0022112080001656
[44] M. Lambert, T. Esch, M. Braun, H. Elasrag, Enhancement of the madabhushi liquid jet in crossflow breakup model by a ligament breakup mechanism, in: 29th Conference on Liquid Atomization and Spray Systems, ILASS–Europe, 2019, pp. 2–4.
[45] T.-H. Shih, W.W. Liou, A. Shabbir, Z. Yang, J. Zhu, A New K-Epsilon Eddy Viscosity Model for High Reynolds Number Turbulent Flows: Model Development and Validation, Tech. rep., 1994.
[46] J. Dai, H. Yu, Numerical and experimental investigations of geometrical parameters on GH2/GO2 injector, Aerosp. Sci. Technol. 106 (2020) 106187. https://doi.org/10.1016/j.ast.2020.106187
[47] A. Akin, H.S. Kahveci, Effect of turbulence modeling for the prediction of flow and heat transfer in rotorcraft avionics bay, Aerosp. Sci. Technol. 95 (2019) 105453. https://doi.org/10.1016/j.ast.2019.105453
[48] G. Faeth, Spray atomization and combustion, 1986. https://doi.org/10.2514/6.1986-136
[49] P.J. O'Rourke, Collective Drop Effects on Vaporizing Liquid Sprays (1981). https://www.osti.gov/biblio/5201366.
[50] Z. Zhang, Y. Yang, Z. Tang, Y. Jin, X. Jin, C. Liu, Experimental study on the droplet size distribution of radial orifice gas–liquid pintle injector at ambient pressure, Exp. Therm. Fluid Sci. 155 (2024) 111178. https://doi.org/10.1016/j.expthermflusci.2024.111178
[51] L. Stumpo, A. Ferrero, L. Maddalena, D. Palmquist, Preliminary Validation and Sensitivity Analysis on a Eulerian/Lagrangian RANS Approach for Liquid Injection in Supersonic Crossflow, 2025. https://doi.org/10.2514/6.2025-1882
[52] K. Radhakrishnan, M. Son, K. Lee, J. Koo, Effect of injection conditions on mixing performance of pintle injector for liquid rocket engines, Acta Astronaut. 150 (2018) 105–116. https://doi.org/10.1016/j.actaastro.2017.12.012
[53] P.-K. Wu, K.A. Kirkendall, R.P. Fuller, A.S. Nejad, Breakup processes of liquid jets in subsonic crossflows, J. Propuls. Power 13 (1) (1997) 64–73. https://doi.org/10.2514/2.5151
[54] J.A. NICHOLLS, A.A. RANGER, Aerodynamic shattering of liquid drops, AIAA J. 7 (2) (1969) 285–290. https://doi.org/10.2514/3.5087
[55] E. Lubarsky, D. Shcherbik, O. Bibik, Y. Gopala, B.T. Zinn, Fuel jet in cross flow - Experimental study of spray characteristics, in: H.W. Oh (Ed.), Advanced Fluid Dynamics, IntechOpen, London, 2012. Ch. 4. https://doi.org/10.5772/26045
[56] V.G. Shaw, P. Elliott, M. Boller, E.J. Gutmark, The breakup and instability structures of liquid jets in subsonic crossflows, Exp. Therm. Fluid Sci. 155 (2024) 111176. https://doi.org/10.1016/j.expthermflusci.2024.111176